


pH-Responsive Mesoporous Silica Nanoparticles Loaded with Naringin for Targeted Osteoclast Inhibition and Bone Regeneration

Shuwei Gong^{1,*}, Shuang Lang^{2,*}, Yan Wang^{3,*}, Xiongfeng Li^{1,*}, Aixian Tian³, Jianxiong Ma³, Xinlong Ma³ 

¹Department of Orthopedics, Huzhou Central Hospital, Zhejiang University Huzhou Hospital, Huzhou, Zhejiang, 313000, People's Republic of China;

²Department of Traditional Chinese Medicine, Huzhou Central Hospital, Zhejiang University Huzhou Hospital, Huzhou, Zhejiang, 313000, People's Republic of China; ³Tianjin Key Laboratory of Orthopedic Biomechanics and Medical Engineering, Orthopedic Research Institute, Tianjin Hospital, Tianjin, 300050, People's Republic of China

*These authors contributed equally to this work

Correspondence: Jianxiong Ma; Xinlong Ma, Tianjin Key Laboratory of Orthopedic Biomechanics and Medical Engineering, Orthopedic Research Institute, Tianjin Hospital, 155 Munan Road, Heping District, Tianjin, 300050, People's Republic of China, Email mjxtianjin@foxmail.com; maxinlong8686@126.com

Background: It is well-established that osteoclast activity is significantly influenced by fluctuations in intracellular pH. Consequently, a pH-sensitive gated nano-drug delivery system represents a promising therapeutic approach to mitigate osteoclast overactivity. Our prior research indicated that naringin, a natural flavonoid, effectively mitigates osteoclast activity. However, naringin showed low oral availability and short half-life, which hinders its clinical application. We developed a drug delivery system wherein chitosan, as gatekeepers, coats mesoporous silica nanoparticles loaded with naringin (CS@MSNs-Naringin). However, the inhibitory effects of CS@MSNs-Naringin on osteoclasts and the underlying mechanisms remain unclear, warranting further research.

Methods: First, we synthesized CS@MSNs-Naringin and conducted a comprehensive characterization. We also measured drug release rates in a pH gradient solution and verified its biosafety. Subsequently, we investigated the impact of CS@MSNs-Naringin on osteoclasts induced by bone marrow-derived macrophages, focusing on differentiation and bone resorption activity while exploring potential mechanisms. Finally, we established a rat model of bilateral critical-sized calvarial bone defects, in which CS@MSNs-Naringin was dispersed in GelMA hydrogel to achieve in situ drug delivery. We observed the ability of CS@MSNs-Naringin to promote bone regeneration and inhibit osteoclast activity in vivo.

Results: CS@MSNs-Naringin exhibited high uniformity and dispersity, low cytotoxicity (concentration $\leq 120 \mu\text{g/mL}$), and significant pH sensitivity. In vitro, compared to Naringin and MSNs-Naringin, CS@MSNs-Naringin more effectively inhibited the formation and bone resorption activity of osteoclasts. This effect was accompanied by decreased phosphorylation of key factors in the NF- κ B and MAPK signaling pathways, increased apoptosis levels, and a subsequent reduction in the production of osteoclast-specific genes and proteins. In vivo, CS@MSNs-Naringin outperformed Naringin and MSNs-Naringin, promoting new bone formation while inhibiting osteoclast activity to a greater extent.

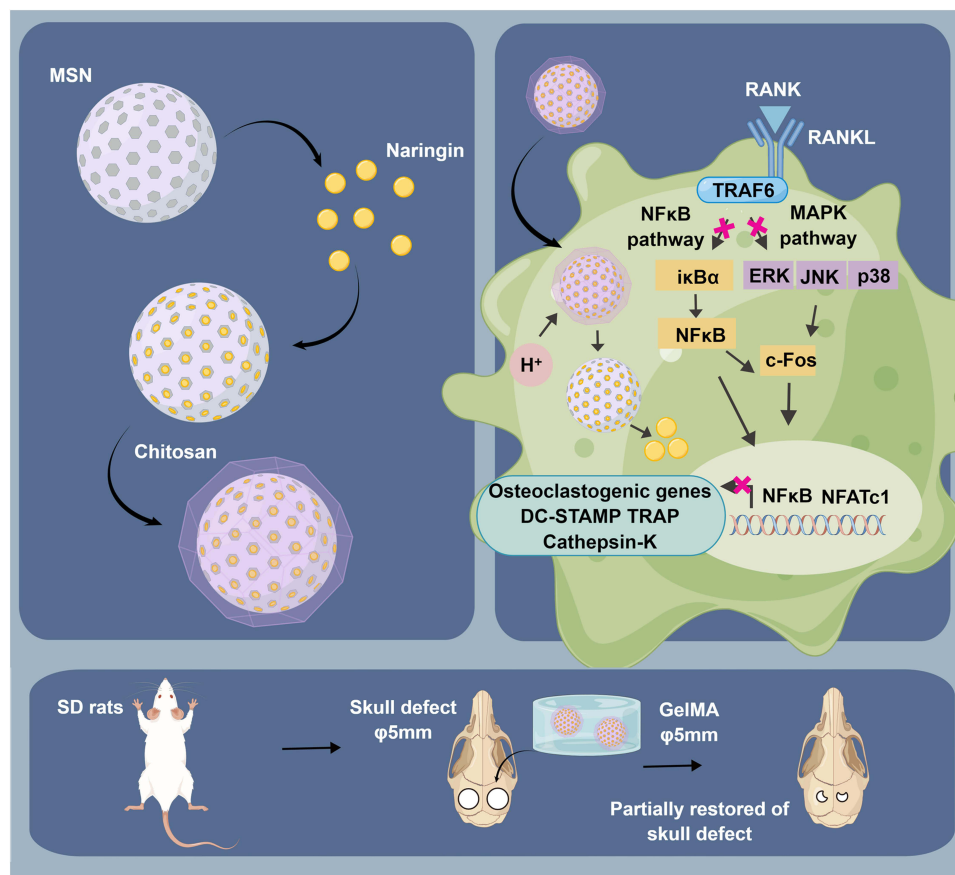
Conclusion: Our research suggested that CS@MSNs-Naringin exhibited the strikingly ability to anti-osteoclasts in vitro and in vivo, moreover promoted bone regeneration in the calvarial bone defect.

Keywords: pH-sensitive gated nano-drug delivery system, mesoporous silica nanoparticles, naringin, chitosan, osteoclast

Introduction

Osteoclasts are giant multinucleated cells (nucleus ≥ 3) formed through the fusion of mononuclear cells that play a pivotal role in bone resorption.^{1,2} Single osteoclasts live for a long time, at least 12 weeks, and about two-thirds of the cells can live up to 24 week.³ The delicate balance between osteoblast-induced bone formation and osteoclast-induced bone resorption is vital for maintaining bone homeostasis.¹ Excessive bone resorption can disrupt the bone microstructure, leading to delayed healing of

Graphical Abstract



bone defects, fractures, and conditions such as osteoporosis, osteoclastoma, and Paget's disease, among others.⁴ Notably, the biology of osteoclasts is closely tied to proton activity. The energy metabolism of osteoclasts is fascinating and complex. In brief, osteoclast differentiation and bone resorption require metabolic reprogramming, which requires a lot of energy and is prone to lactic acid accumulation.^{5,6} Besides, they dissolve bone matrix by secreting H⁺ into the sealing lacuna through vacuolar H⁺-ATPase (V-ATPase) during bone resorption. In turn, some of the released H⁺ is then reabsorbed into the cell from the sealing lacuna, resulting in periodic H⁺ oscillations and gradual cytoplasm acidification.⁷ Additionally, specific organelles are acidic, such as endosomes (pH: 4.9–6.0) and lysosomes (pH: 4.0–4.5), which are responsible for endocytosis of nanoparticles into osteoclasts.^{8,9} This characteristics of acidic microenvironmental of osteoclasts underscores the potential of pH-sensitive gated drug delivery systems as a therapeutic strategy for conditions characterized by excessive bone resorption.

Traditional osteoclast inhibitors include bisphosphonates, denosumab, estrogen, and selective estrogen receptor modulators.¹⁰ However, it is now recognized that the use of conventional osteoclast inhibitors may bring potential risks, including jaw osteonecrosis or femoral neck fractures.¹¹ More recently, natural compounds have emerged as promising osteoclast inhibitors, including glabridin,¹² protocatechuic acid,¹³ hesperetin,¹⁴ galangin,¹⁵ eupatilin,¹⁶ and others. Naringin, a natural flavonoid, is known for its anti-inflammatory and antioxidant properties, benefiting conditions such as cancer, cardiovascular diseases, and neurodegenerative disorders.¹⁷ In the musculoskeletal system, naringin (100 µg/mL) enhances osteoblast differentiation by upregulating BMP-2 expression through the Wnt/β-catenin signaling pathway.¹⁸ More importantly, our previous research confirmed its (20 ng/mL) ability to reduce osteoclast differentiation^{19,20} and promote osteoclast mitochondria-mediated apoptosis.²⁰ Despite these advantages, naringin is

hindered by poor solubility (in water 500 µg/mL), low bioavailability (<5%), and a short half-life. Intelligent drug delivery system provides a solution to the above predicaments.^{21,22}

Porous silica nanoparticles possess unique attributes, such as a large specific surface area, substantial pore volume, ease of modification, and excellent biocompatibility.²³ Among them, mesoporous silica nanoparticles (MSNs), with pore sizes ranging from 2 to 50 nm, represent prime candidates for drug delivery and biomedical applications and have earned recognition as “Generally Recognized As Safe” by the Food and Drug Administration (FDA).²⁴ Consequently, MSNs hold significant promise for clinical applications.²⁵ Previous studies have shown that mesoporous silica can effectively deliver natural flavonoids to inhibit osteoclast generation, but this drug delivery system lacks environmental responsiveness.²⁶ To address concerns about the premature release of loaded drugs en route to their target within MSNs and to enhance responsiveness to pH stimulation, chitosan, serving as a “gatekeeper”, meets these requirements.²⁷ Chitosan (CS) undergoes protonation of amino groups on its molecular skeleton under acidic conditions, rendering it pH-sensitive.²⁷ A previous study developed CS@MSNs drug delivery microspheres based on the acidic tumor microenvironment (pH 6.5–6.8) to increase drug release to breast cancer cells, thereby improving drug dosage and inducing cancer cell death.²⁸ This is similar to the conceptualization of the present study. However, the effects of chitosan@MSNs in delivering antiresorptive drugs on osteoclast differentiation and function, along with the underlying signaling mechanisms, remain unexplored. Considering the acid-dependence of osteoclasts activity, using naringin, a natural product, as an effective ingredient to synthesize acid-sensitive nano-gating materials to intelligently inhibit the function of osteoclasts, and exploring its mechanism of action is the innovation of this study. Given this research background, our study focused on developing a pH-sensitive gating system using chitosan-coated mesoporous silica nanoparticles loaded with naringin (CS@MSNs-Naringin). To confirm the above hypothesis, BMMs were used to induce osteoclasts and co-cultured with CS@MSNs-Naringin to observe their ability to inhibit osteoclasts in vitro. The ability to inhibit osteoclasts and promote bone regeneration in vivo was observed by CS@MSNs-Naringin implantation into a rat model of bone defect.

Material and Methods

Synthesis of MSNs, MSNs-Naringin, CS@ MSNs and CS@MSNs-Naringin

During the synthesis process, the methods described by Tang et al²⁹ were adopted with some modifications. Initially, 1 g of cetyltrimethylammonium bromide (CTAB)(Aladdin, Shanghai, China) was dissolved in 480 mL of distilled water containing 0.28 g of NaOH, stirred at 80 °C for 30 min, and then 5 mL of tetraethyl orthosilicate (TEOS) (Aladdin, Shanghai, China) was added dropwise. Stirring was continued for 2 hours at 80 °C. The resulting solution was centrifuged, washed with distilled water and ethanol, and dried under vacuum to obtain CTAB-MSNs. To remove the templating agent, 1 g of CTAB-MSNs was placed in a mixture of 120 mL of ethanol and 15 mL of hydrochloric acid and refluxed for 12 hours. The obtained samples were vacuum-dried for 12 hours to yield MSNs.

To prepare CS@MSNs, 250 mg of chitosan (Aladdin, Shanghai, China) was dissolved in 50 mL of a 3% acetic acid solution and stirred for 24 hours to obtain a 0.5% w/v chitosan solution. Then, 200 mg of MSNs was evenly dispersed in the chitosan solution, and the mixture was stirred for 36 hours. The resulting material was washed and vacuum-dried to obtain CS@MSNs.

To prepare MSNs-Naringin, a 30 mg/mL naringin (Product No. 71,162, Sigma-Aldrich, St. Louis, MO, USA) solution was prepared in dimethyl sulfoxide (DMSO). 250 mg of MSNs were added to the solution, and the mixture was stirred in the dark for 24 hours. The MSNs encapsulated with naringin (MSNs-Naringin) were obtained after centrifugation and vacuum drying. Next, 250 mg of chitosan was dissolved in 50 mL of a 3% acetic acid solution and stirred for 24 hours to obtain a 0.5% w/v chitosan solution. Then, 200 mg of MSNs-Naringin was evenly dispersed in the chitosan solution, and the mixture was stirred for 36 hours. The resulting material was washed and vacuum-dried to obtain CS@MSNs-Naringin.

Characterization

The morphology and mesoporous structure of nanoparticles were observed by transmission electron microscope (TEM) (JEOL, Tokyo, Japan) at a voltage of 200 kV. Scanning electron microscopy (SEM) (Hitachi, Hitachi, Japan) was used to observe the morphology of the synthesized nanomaterials. The zeta potential was adopted to measure the charge of

nanoparticles by dynamic light scattering (Microtrac MRB, Osaka, Japan). Surface area and pore volume were analyzed by nitrogen adsorption-desorption measurement through Brunauer-Emmett-Teller (BET) and Barrett-Joyner-Halenda (BJH) method (Micromeritics, Norcross, GA, USA). Thermo gravimetric (TGA) analysis was performed on a TGA-DSC 3+ (METTLER TOLEDO, Zurich, Switzerland) at a 20°C/min heating rate under a nitrogen atmosphere. Fourier transform infrared spectrophotometric (FT-IR) spectra were tested by an FT-IR spectrometer (ThermoFisher, Waltham, MA, USA). X-ray photoelectron spectroscopy (XPS) analysis of different nanomaterials was performed by the Escalab 250Xi X-ray photoelectron spectrometer (ThermoFisher, Waltham, MA, USA). FEI-Talos-f200x was used to complete the TEM-EDS (ThermoFisher, Waltham, MA, USA).

Loading and Release Efficacies of Naringin

The loading efficiency was evaluated using two methods.²⁶ The first method involved measuring the absorbance value of the collected supernatant at 284 nm with a UV-visible spectrophotometer to calculate the encapsulation efficiency (EE): $EE(\%) = W_{\text{naringin in MSNs}} / W_{\text{naringin fed initially}} \times 100\%$. The second method involved calculating the difference in weight reduction between MSNs and MSNs-Naringin using TGA: $LE = W_{\text{naringin in MSNs-Naringin}} / W_{\text{MSNs-Naringin}} \times 100\%$.

To investigate the release of Naringin from CS@MSNs-Naringin, phosphate buffer (PBS) solutions with pH values of 7.4 or 5.6 were used as simulated release media. CS@MSNs-Naringin (30 mg) were placed in a 10,000 Da dialysis bag (Yuanye, Shanghai, China) immersed in the release medium (30 mL) with constant stirring. At periodic intervals, 5 mL of the medium was removed to determine Naringin concentration using High Performance Liquid Chromatography (HPLC), and an equal volume of fresh medium was added simultaneously. The cumulative release rate of Naringin from CS@MSNs-Naringin at different time points was calculated and recorded.

Synthesis of CS@MSNs- Rhodamine B (RhB)

To demonstrate that CS@MSNs-Naringin can be endocytosed by osteoclasts and pre-osteoclasts, red fluorescent CS@MSNs-RhB nanospheres, with Rhodamine B (RhB) replacing Naringin, were prepared. A RhB solution (1 mg/mL) was prepared by dissolving RhB (MedChemExpress, NJ, USA) in distilled water. MSNs (60 mg) were added to 20 mL of RhB aqueous solution, stirred for 36 hours at room temperature under dark conditions, washed with distilled water, and collected by centrifugation. The final product was dried under a vacuum to obtain MSNs-RhB. Subsequently, 40 mg of MSNs-RhB were evenly dispersed in 10 mL of a 0.5% w/v chitosan solution, stirred for 36 hours under dark conditions, washed, and vacuum-dried to obtain CS@MSNs-RhB.

Bone Marrow-Derived Macrophages (BMMs) Extract and Culture

The femur and tibia of 8-week-old C57/BL6 mice were aseptically isolated. The bone marrow was flushed out using a washing medium (99% α -MEM + 1% penicillin/streptomycin). Subsequently, the bone marrow cells were centrifuged and lysed with 5 mL of red blood cell lysate at a low temperature for 10 minutes. The collected cells were cultured in T75 flasks overnight using culture medium (89% α -MEM + 10% FBS + 1% penicillin/streptomycin). The suspended cells were collected by centrifugation, followed by their culture in T75 flasks with an inducing medium (89% α -MEM + 10% FBS + 1% penicillin/streptomycin + 50 ng/mL M-CSF) for 5 days to obtain BMMs.³⁰

Cytotoxicity Assay in vitro

BMMs were evenly seeded in 96-well plates with differentiation medium (89% α -MEM + 10% FBS + 1% penicillin/streptomycin + 100 ng/mL RANKL + 50 ng/mL M-CSF). In these plates, different concentrations of MSNs, Naringin, MSNs-Naringin, or CS@MSNs-Naringin were co-cultured in the differentiation medium with concentration gradients. After 24, 48, and 72 hours of co-culture, a fresh culture medium containing 10% Cell Counting Kit-8 (CCK-8; Biosharp, Hefei, China) was applied. The absorbance was measured at 450 nm after a 1-hour incubation in the dark. Similarly, MC3T3-E1 cells, provided by ATCC, were evenly seeded in 96-well plates and cultured in a culture medium (89% α -MEM + 10% FBS + 1% penicillin/streptomycin). The intervention and detection methods were consistent with those described above.

Concentration gradients for MSNs, MSNs-Naringin, and CS@MSNs-Naringin were set at 10, 20, 40, 80, 120, and 160 µg/mL. The concentration gradient for Naringin was set at 1.875, 3.75, 7.5, 15, 30, 60, and 120 µM, respectively.

After establishing a safe dose of the drug or nanomaterial using the CCK-8 assay, live/dead staining (Solarbio, Beijing, China) was employed to verify the biosafety of CS@MSNs-Naringin for BMMs.

Intracellular Uptake of CS@MSNs-RhB

BMMs were uniformly seeded in 24-well plates with differentiation medium, and the medium was changed every other day. After 6 days, the differentiation medium containing 15 µg/mL or 30 µg/mL CS@MSNs-RhB was added. After a 24-hour co-culture, the cells were fixed with 4% paraformaldehyde, permeabilized with 0.1% Triton X-100 for 3–5 minutes, and then incubated with iFluor™ 488 phalloidin solution (Yeasen, Shanghai, China) for 1 hour in the dark. Subsequently, the cells were washed, and the nuclei were counterstained with a DAPI solution. The endocytosis of nanomaterials was observed under a confocal fluorescence microscope (Olympus, Tokyo, Japan).

Tartrate-Resistant Acid Phosphatase (TRAP) Staining

BMMs were evenly seeded in 24-well plates with or without 80 µg/mL MSNs, Naringin, MSNs-Naringin, and CS@MSNs-Naringin in a differentiation medium, changed every other day without nanoparticles and drugs. After 7 days of differentiation, the cells were fixed with 4% paraformaldehyde. Subsequently, the cells were stained using a TRAP staining kit (Solarbio, Beijing, China) following the provided procedure, and the positive cells were identified as multinucleated cells with three or more nuclei.

Observation of F-Actin Rings

BMMs were processed in the same manner as the TRAP staining. After differentiation, the cells were fixed with 4% paraformaldehyde, permeabilized the cell membrane with 0.1% Triton X-100 for 3–5 minutes, and then incubated with iFluor™ 488 phalloidin solution (Yeasen, Shanghai, China) for 1 hour in the dark. Subsequently, the cells were washed, and the nuclei were counterstained with a DAPI solution. F-actin rings were observed using a confocal fluorescence microscope.

Observation of Bone Resorption Pits

BMMs were uniformly planted in 96-well plates covered with bovine cortical bone slices (IDS, Brighton, UK) with or without MSNs, Naringin, MSNs-Naringin, and CS@MSNs-Naringin in differentiation medium. The differentiation medium was changed every other day without nanoparticles and drugs. After 7 days of differentiation, the bovine cortical bone slices were removed from the 96-well plates, and the surface cells were removed by ultrasound. Subsequently, the bone resorption pits were observed using scanning electron microscopy (Hitachi, Hitachi, Japan).

Real-Time PCR Analysis

BMMs were evenly seeded in six-well plates with or without MSNs, Naringin, MSNs-Naringin, and CS@MSNs-Naringin in a differentiation medium. The medium was changed every other day without nanoparticles and drugs. After 7 days, the cells were lysed with TRIzol reagent (Invitrogen, Carlsbad, CA, USA) to extract total RNA using isopropyl alcohol and chloroform, followed by quantification using NanoDrop (ThermoFisher, Waltham, MA, USA). The First Strand cDNA Synthesis Kit (Roche, Basel, Switzerland) was used to synthesize cDNA, followed by the SYBR Premix Ex Taq II Kit (TaKaRa) as the Real-Time PCR reaction system. GAPDH was selected as the endogenous control. The real-time PCR primer sequences for c-Fos, TRAP, Cathepsin-K, DC-STAMP, NFATc-1, and GAPDH (Sangon, Shanghai, China) are listed in [Supplementary Table 1](#).

Western Blot Analysis

Interventions for BMMs were the same as those in real-time PCR analysis. Briefly, cells were lysed with RIPA on ice to extract total protein, and the extracted protein concentration was measured using a BCA protein assay kit (Beyotime,

Shanghai, China). SDS-PAGE gels were prepared for protein separation based on molecular weight. Proteins of specific molecular weights were then transferred to PVDF membranes, which were incubated with primary antibodies overnight and secondary antibodies for 2 hours the next day. The protein expression was detected using the Amersham Imager 600 imaging system (GE, Fairfield, CT, USA).

The primary antibodies included anti-p-ERK, ERK, p-JNK, JNK, p-p38, p38, c-Fos (Cell Signaling Technology, Danvers, MA, USA), p-NF- κ B, p-I κ B α , I κ B α , Bcl-2, Bax, Cleaved caspase-3, β -actin, β -tubulin (Abcam, Cambridge, UK), NF- κ B, NFATc1 (SANTA, Dallas, TX, USA).

Immunofluorescence Analysis

BMMs were evenly seeded in cell culture dishes (ϕ 25 mm; NEST, Wuxi, China), and the intervention method was the same as for the real-time PCR analysis. After 7 days, the cells were fixed with 4% paraformaldehyde for 30 minutes, and the cytomembrane permeability was increased by 3% Triton X-100. The cells were blocked with non-immune animal serum for 40 minutes, after which the primary antibodies NFATc1 (SANTA, Dallas, TX, USA) were added and incubated overnight at 4°C. The next day, the primary antibodies were removed, and the secondary antibodies were incubated with the cells for 1 hour. DAPI was used to counterstain the nuclei, F-actin was stained with phalloidin, and the fluorescence intensity was observed by a confocal fluorescence microscope.

TUNEL Assay

BMMs were processed the same way as for the “Immunofluorescence analysis”. To further detect the level of apoptosis of osteoclasts and pre-osteoclasts, the TUNEL apoptosis assay kit (Beyotime, Shanghai, China) was used to label DNA fragments. The cells were then immediately viewed using a confocal fluorescence microscope at an excitation wavelength of 550–570 nm and photographed. TUNEL-positive cells were labeled with red fluorescence.

Synthesis and characterization of Gelatin Methacryloyls (GelMA) Hydrogels with CS@MSNs-Naringin

A GelMA hydrogel containing nanoparticles was specially prepared to achieve the in situ release of nanoparticles in bone defects. GelMA hydrogels were purchased from EFL Co., Ltd (Suzhou, China), and a 5% w/v GelMA hydrogel solution was prepared according to its working manual.³¹ Ten milligrams of MSNs, Naringin, MSNs-Naringin, and CS@MSNs-Naringin were respectively dispersed by ultrasonication in 10 mL of GelMA solution. Liquid GelMA was solidified using a portable UV light (405 nm).

The hydrogel was placed at -20°C for 6 hours and -80°C for 2 hours and then dried in a freeze-dryer for 18 hours. After full drying, the hydrogel was weighed as W_o . The hydrogel was immersed in PBS at 37°C for 24 hours. The moisture was wiped, and it was weighed as W_t . The swelling rate was calculated using the formula: Swelling rate = $(W_t - W_o) / W_o \times 100\%$. For the degradation rate, the hydrogel was fully dehydrated, and its weight was recorded as W_o . Then, it was immersed in PBS at 37°C for 7, 14, and 28 days, and the weight at each time point was recorded. The degradation rate formula is as follows: Degradation rate = $(W_o - W_t) / W_o \times 100\%$. To test the mechanical properties of the hydrogel, a diameter of 2.5cm and a height of 1cm hydrogel was prepared ($n=3$). The mechanical property was measured by a mechanical tester (Shimadzu, Kyoto, Japan), and the strain rate was 1 mm/min. Subsequently, the stress-strain curve was plotted.

The morphology of GelMA and the dispersion of CS@MSNs-Naringin were detected by scanning electron microscopy (SEM) using SU-70 (Hitachi, Hitachi, Japan). GelMA and GelMA containing CS@MSNs-Naringin were injected into molds of different shapes and solidified for 2 minutes under the irradiation of an ultraviolet light source to observe the shape plasticity of these two hydrogel materials. Si elemental mapping of GelMA containing nanoparticles was performed by the FEI-Talos-f200x (ThermoFisher, Waltham, MA, USA).

To investigate the release of naringin in GelMA+CS@MSNs-Naringin. GelMA+CS@MSNs-Naringin (1 mg/mL) with a diameter of 5mm and a thickness of 2mm (the size of vivo implant) was wrapped in a 1 kD dialysis bag in 1 μg /mL collagenase II /PBS solution (10 mL) at 37°C and 60 rpm for drug release. At predetermined intervals, 2 mL of

medium outside the dialysis bag was removed and an equal volume of new solution was added, and drug release was calculated using HPLC.

Grouping and Establishment of a Calvarial Bone Defect Rat Model

Animal experiments were approved by the Animal Ethics Committee of Tianjin Hospital (2022 205). All applicable institutional and governmental regulations concerning the ethical use of animals were followed. Male rats (Institute of Genetics and Developmental Biology, Chinese Academy of Sciences, Beijing, China) at 8 weeks of age underwent bilateral calvarial bone defect surgery with a critical size of 5 mm to evaluate the bone regeneration performance of CS@MSNs-Naringin. A total of 30 rats were randomly divided into 6 groups: (1) Control group (bilateral defects were not filled with hydrogel), (2) GelMA group (bilateral defects were filled with GelMA hydrogels), (3) MSNs group (bilateral defects were filled with GelMA hydrogels containing 1 mg/mL MSNs), (4) Naringin group (bilateral defects were filled with GelMA hydrogels containing 1 mg/mL Naringin), (5) MSNs-Naringin group (bilateral defects were filled with GelMA hydrogels containing 1 mg/mL MSNs-Naringin), and (6) CS@MSNs-Naringin group (bilateral defects were filled with GelMA hydrogels containing 1 mg/mL CS@MSNs-Naringin).

The rats were anesthetized by intraperitoneal injection of pentobarbital (4 mg/100 g). After being fixed in a prone position, a 2 cm sagittal incision was made in the middle of the scalp. The rat calvarial bone was exposed after bluntly separating the muscle and periosteum. Subsequently, a 5 mm diameter defect was drilled along both sides of the midline of the calvarial bone. The defect was filled with or without the corresponding sterilized hydrogel and solidified by irradiation with a portable UV light (405 nm). The wound was sutured layer by layer. Eight weeks after implantation, the rats were euthanized with an anesthetic overdose to obtain calvarial bone and other organ specimens.

Micro-CT

The Inveon micro PET/CT (Siemens, Berlin, Germany) was used to scan the cranial bones with a scanning voltage of 80 kV and a current of 500 μ A from the front to the end of the cranium, with a spatial resolution of 10 μ m. Subsequently, the Inveon analysis workstation was used to reconstruct the 3D structure. The region of interest (ROI) was determined as a regular cylinder with a fixed size, 5 mm in diameter, and consistent with the position of the defect drilled during modeling. Bone volume/total volume (BV/TV), bone surface area/bone volume (BSA/BV), trabecular separation (Tb.Sp), trabecular number (Tb.N), and trabecular thickness (Tb.Th) were collected and calculated.

Hematoxylin/Eosin (HE), Goldner Trichrome, TRAP, and Immunohistochemistry (IHC) Staining

The cranial bones were fixed with 4% paraformaldehyde overnight, decalcified with 0.5M EDTA for 1 month, embedded in paraffin, and sectioned to 5 μ m. HE, Goldner trichrome, and TRAP staining were performed following the respective guidelines. HE staining of organs was carried out similarly to that of cranial bones but without decalcification.

For IHC staining, 10 mM sodium citrate buffer was used for antigen retrieval, and sections were subsequently blocked with serum. They were incubated with NFATc1 (SANTA, Dallas, TX, USA) and c-Fos (Cell Signaling Technology, Danvers, MA, USA) primary antibodies at 4°C overnight. The next day, the sections were incubated with secondary antibodies at room temperature for 30 minutes. Sections were stained with 3,3'-diaminobenzidine and counterstained with a hematoxylin dye solution. The quantification of IHC was performed using Image J (NIH, Bethesda, USA).

TUNEL Staining

Sections were deparaffinized in xylene for 5–10 minutes. Repeat two times. 20 μ g/mL of proteinase K without DNase was incubated at 20–37 °C for 15–30 min. The sections were washed three times with PBS. The prepared TUNEL solution was dropped into the sections and incubated at 37 °C in the dark for 60 minutes. The cells were washed three times with PBS. The nuclei were stained with DAPI.

Statistical Analysis

Results were presented as mean \pm standard deviation (SD). A one-way ANOVA was used for comparisons of three or more groups, followed by the least significant difference (LSD) method for between-group comparisons (SPSS 21; IBM, Armonk, NY, USA). P-values < 0.05 were considered statistically significant.

Results

Synthesis and Characterization of MSNs, CS@MSNs, MSNs-Naringin, and CS@MSNs-Naringin

TEM images revealed that the MSNs had a uniform, round shape, were homogeneously dispersed, and exhibited clear mesoporous structures. After coating with chitosan, CS@MSNs and CS@MSNs-Naringin had a smooth surface and retained its round shape, although it showed some loss of surface pore structure ([Figure 1A](#) and [Supplementary Figure 1A](#)). Moreover, the thickness of the CS shell was 14.17 ± 1.66 nm ([Supplementary Figure 1B](#)). SEM images confirmed that MSNs, CS@MSNs, MSNs-naringin and CS@MSNs-Naringin all exhibited a uniform spherical shape. Due to the coating of chitosan, the particle sizes of CS@MSNs and CS@MSNs-Naringin were slightly increase ([Supplementary Figure 1C](#) and [Table 1](#)). Brunauer–Emmett–Teller analysis demonstrated that MSNs had a substantial surface area of $919.284 \text{ m}^2/\text{g}$ and a pore volume of 0.815 cc/g , with a type IV isotherm for mesoporous materials. In comparison, MSNs-Naringin exhibited values of $388.783 \text{ m}^2/\text{g}$ and 0.557 cc/g , while CS@MSNs-Naringin showed values of $155.76 \text{ m}^2/\text{g}$ and 0.258 cc/g , confirming successful drug loading and chitosan coating ([Figure 1B](#)). The zeta potential changed from $-30.2 \pm 0.391 \text{ mV}$ for MSNs to $-35.7 \pm 1.025 \text{ mV}$ for MSNs-Naringin and $27.9 \pm 1.284 \text{ mV}$ for CS@MSNs-Naringin due to the positive charge of chitosan ([Figure 1C](#)).

FITR spectroscopy further confirmed the loading of naringin in MSNs-Naringin and CS@MSNs-Naringin. Naringin displayed characteristic peaks at 1644.69 cm^{-1} and 3418.52 cm^{-1} , while MSNs-Naringin exhibited corresponding peaks at 1640.99 cm^{-1} and 3422.45 cm^{-1} . In the case of CS@MSNs-Naringin, characteristic peaks of naringin appeared at 1638.59 cm^{-1} and 3425.97 cm^{-1} , providing evidence of successful assembly of naringin into both MSNs-Naringin and CS@MSNs-Naringin ([Figure 1D](#)). UV-Vis analysis suggested that the encapsulation efficiency of naringin was $27.96\% \pm 0.98\%$. TGA revealed that the loading efficiency of naringin in MSNs-Naringin was $23.16\% \pm 1.36\%$, and CS@MSNs-Naringin was $14.98\% \pm 1.53\%$ ([Figure 1E](#)). Moreover, TGA showed that the encapsulation amount of CS was $14.26\% \pm 1.31\%$. CS@MSNs-Naringin exhibited significant acid sensitivity, with naringin release rates of $52.61\% \pm 1.43$ at pH 5.6 and $22.81\% \pm 1.62$ at pH 7.4 in PBS solution during a drug release test ([Figure 1F](#)).

XPS characterization was performed to analyze the samples' surface composition further. According to [Figure 1G](#), the full spectrum data of all samples exhibit characteristic peaks located at 533.08 eV, 284.08 eV, and 103.08 eV, corresponding to the presence of O 1s, C 1s, and Si 2p signals, respectively. In the Si 2p, O 1s, C 1s energy spectrum, Si and O both show the changing trend of MSNs and MSNs-naringin > CS@MSNs and CS@MSNs-Naringin. In contrast, C shows the opposite trend, which indicates that chitosan has successfully coated mesoporous silicon ([Figure 1G](#)). TEM-EDS also confirmed the above phenomenon, after the CS coating of CS@MSNs and CS@MSNs-Naringin, the surface Si element and O element decreased, while the C element increased ([Supplementary Figure 1D](#)).

Evaluation of Biosafety and Endocytosis of Nanoparticles in vitro

The safety of biomaterials is essential for their applications. To assess the cytotoxicity of MSNs, Naringin, MSNs-Naringin, and CS@MSNs-Naringin on BMMs and MC3T3-E1 cells, CCK8 assays were conducted at 24, 48, and 72 hours. The maximum safe concentration of MSNs and MSNs-Naringin was determined to be $80 \text{ }\mu\text{g/mL}$ for both BMMs and MC3T3-E1, while CS@MSNs-Naringin showed a safe concentration of $120 \text{ }\mu\text{g/mL}$ for these cell types, which may be attributed to the superior biocompatibility of chitosan ([Figure 2A](#) and [Supplementary Figure 2A](#)). Furthermore, Naringin did not significantly inhibit the proliferation of BMMs at concentrations up to $120 \text{ }\mu\text{M}$ and MC3T3-E1 at concentrations up to $60 \text{ }\mu\text{M}$, as demonstrated by CCK8 assays ([Supplementary Figure 2B](#) and [C](#)). Accordingly, the intervention doses for MSNs, Naringin, Naringin-MSNs, and CS@MSNs-Naringin were set at $80 \text{ }\mu\text{g/mL}$ (within $60 \text{ }\mu\text{M}$). The biosafety of CS@MSNs-Naringin with $80 \text{ }\mu\text{g/mL}$ was further confirmed through dead/alive staining ([Supplementary Figure 2D](#)).

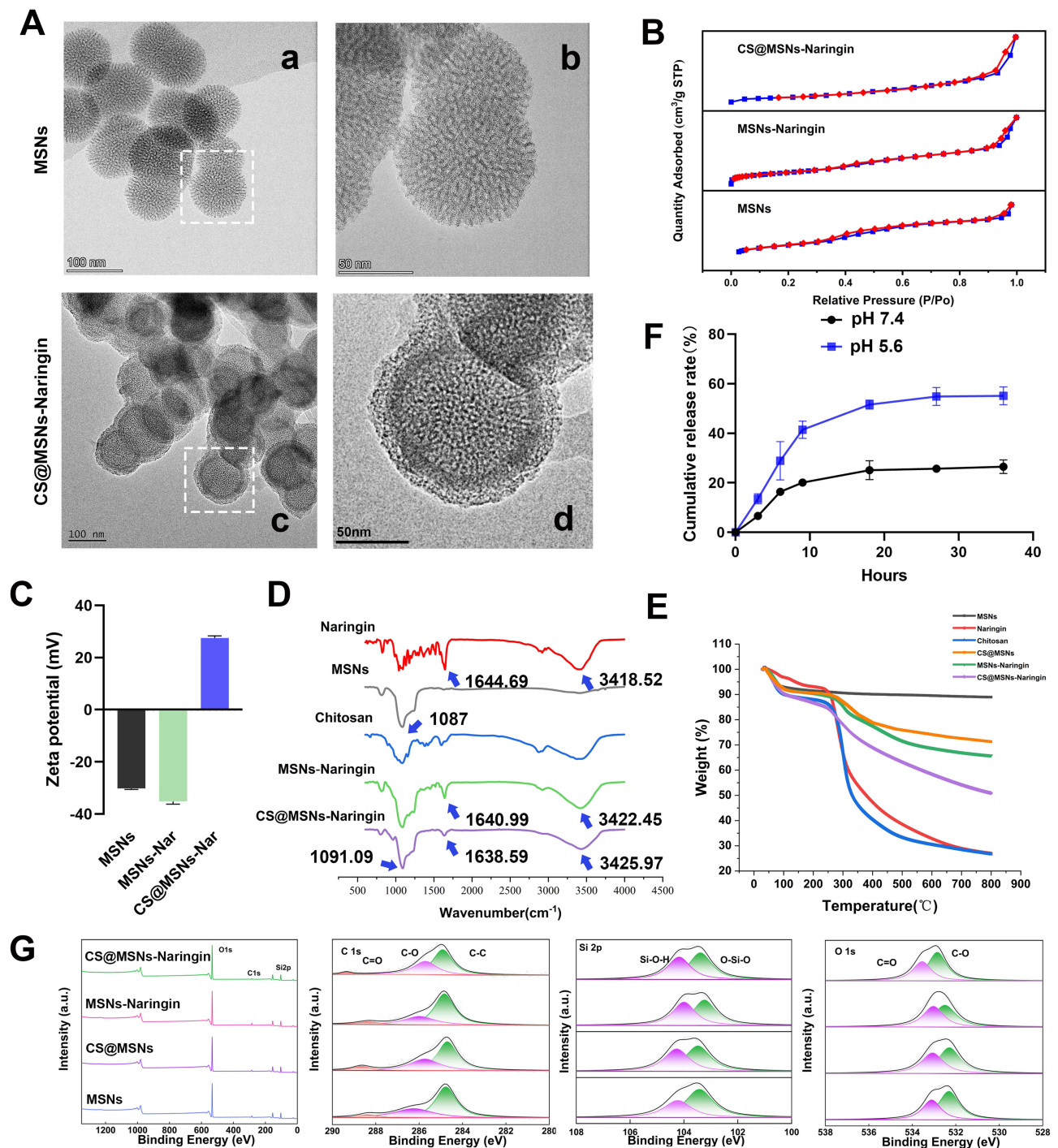


Figure 1 Characterization of MSNs, CS@MSNs, MSNs-Naringin, and CS@MSNs-Naringin. **(A)** The TEM images of MSNs and CS@MSNs-Naringin, (a) MSNs, 100nm Scale bar, (b) MSNs, 50nm Scale bar, (c) CS@MSNs-Naringin, 100nm Scale bar, (d) CS@MSNs-Naringin, 50nm Scale bar. **(B)** The BET images of MSNs, MSNs-Naringin, and CS@MSNs-Naringin. **(C)** The Zeta potential of MSNs, MSNs-Naringin (MSNs-Nar) and CS@MSNs-Naringin (CS@MSNs-Nar) (n=3). **(D)** The FTIR spectra of Naringin, MSNs, Chitosan, MSNs-Naringin, and CS@MSNs-Naringin. **(E)** The TGA thermograms of Naringin, MSNs, Chitosan, CS@MSNs, MSNs-Naringin, and CS@MSNs-Naringin. **(F)** The cumulative percentage release of naringin from CS@MSNs-Naringin at different pH (n=3). **(G)** The XPS of MSNs, CS@MSNs, MSNs-Naringin, CS@MSNs-Naringin.

To demonstrate that CS@MSNs-Naringin can be endocytosed by osteoclasts and pre-osteoclasts, CS@MSNs-RhB nanospheres, with Rhodamine B (RhB) replacing Naringin, were prepared. Confocal microscopy showed that CS@MSNs-Nar was internalized by osteoclasts and pre-osteoclasts in a dose-dependent manner after 24 hours of co-culture (Figure 2B).

Table I The Surface Area, Volume of Pores, Pore Diameter, Particle Size and Zeta Potential of MSNs, CS@MSNs, MSNs-Naringin and CS@MSNs-Naringin

	Surface area (m ² /g)	Volume of pores (cc/g)	Pore diameter (nm)	Particle size (nm)	Zeta potential (mV)
MSNs	919.284	0.815	2.056	128.85±1.21	-30.2±0.391
CS@MSNs	163.328	0.226	—	137.38±0.95	32.68±1.537
MSNs-Naringin	388.783	0.557	0.933	119.77±1.79	-35.7±1.025
CS@MSNs-Naringin	155.76	0.258	—	144.48±0.52	27.9±1.284

Effects of CS@MSNs-Naringin on Osteoclastogenesis and Bone Resorptive Activity

Osteoclastogenesis involves several stages, including cell proliferation, fusion, polarization, and the formation of F-actin rings. TRAP staining is the gold standard for identifying osteoclast formation.^{2,32} Mature osteoclasts appeared as large multinucleated cells, stained in purple-red with TRAP. MSNs-Naringin and CS@MSNs-Naringin significantly inhibited osteoclastogenesis, with CS@MSNs-Naringin showing the most prominent inhibitory effect (Figure 3A). The formation of F-actin rings, crucial for osteoclasts' bone-resorptive function, was also effectively inhibited by CS@MSNs-Naringin compared to MSNs-Naringin (Figure 3B).

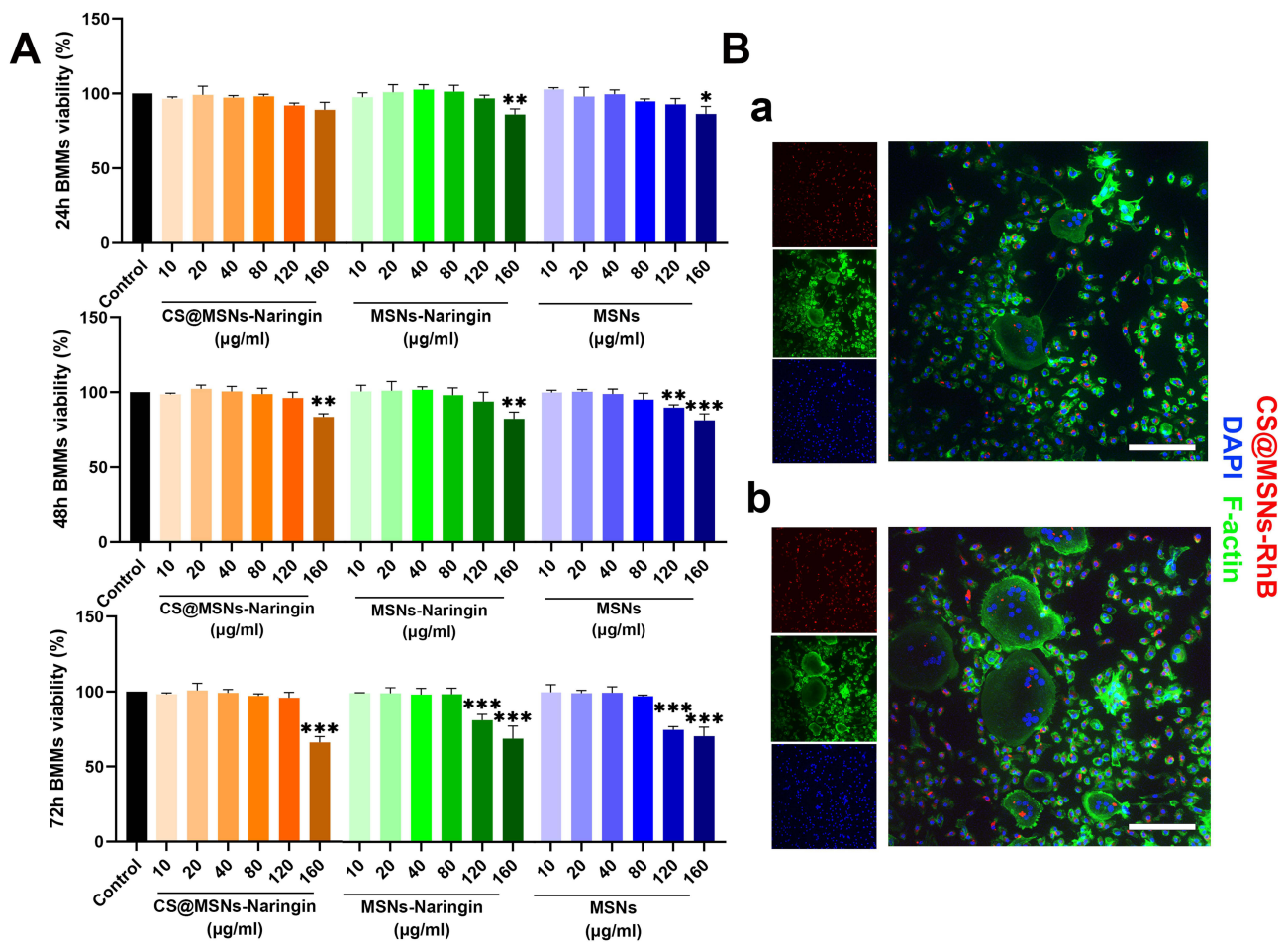


Figure 2 Cytotoxicity of nanoparticles and the endocytosis ability of CS@MSNs-RhB. **(A)** Cytotoxicity of CS@MSNs-Naringin, MSNs-Naringin, and MSNs to BMMs at 24, 48, 72h. The data were expressed as mean±standard deviation and calculated by One Way AONVA. *: $p<0.05$; **: $p<0.01$; ***: $p<0.001$ compared to the control group. **(B)** Effect of CS@MSNs-RhB intervention 24h at 6 days of BMMs differentiation: (a) The concentration of CS@MSNs-RhB was 15µg/mL, (b) The concentration of CS@MSNs-RhB was 30µg/mL. Scale bar = 100 µm.

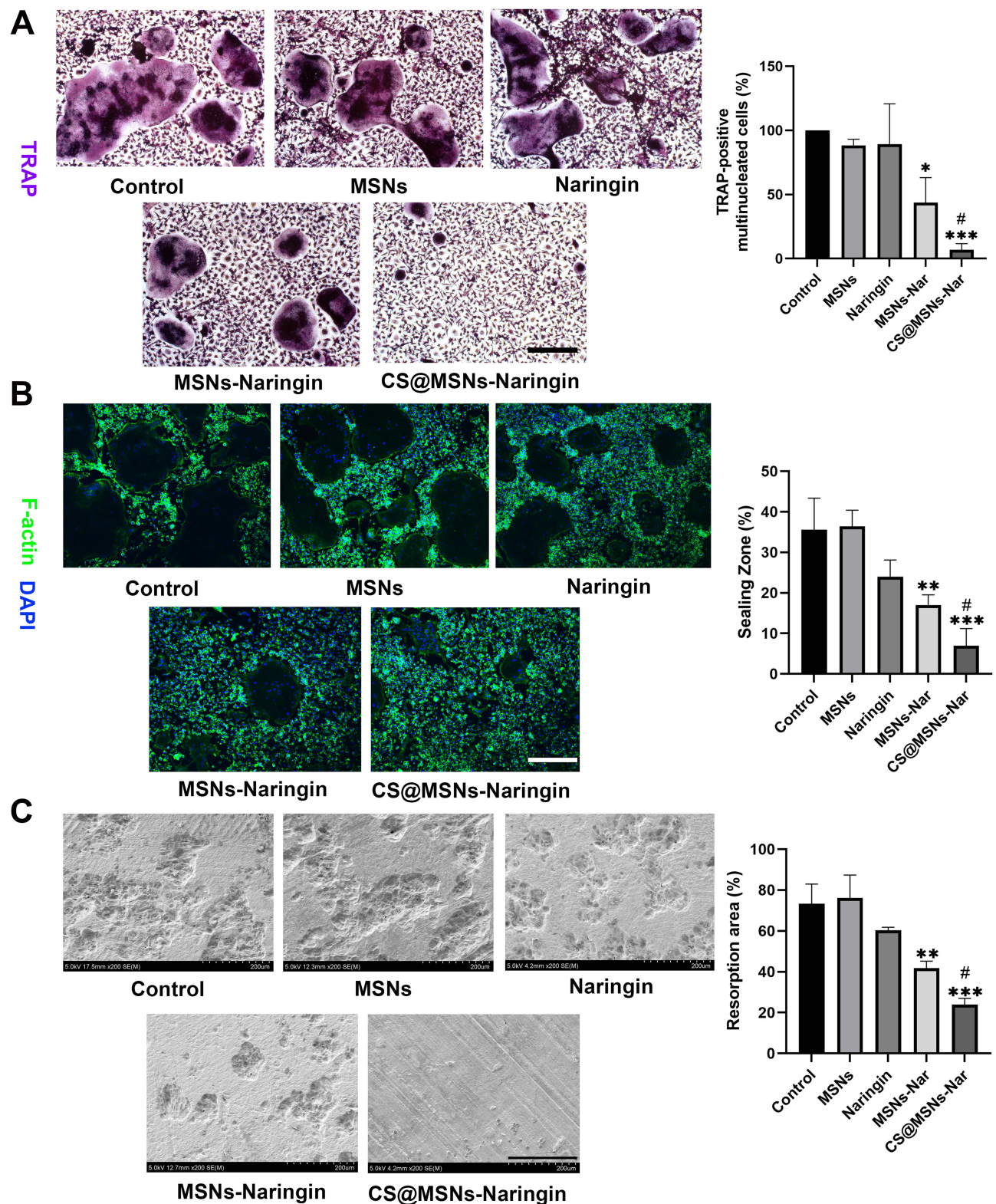


Figure 3 CS@MSNs-Naringin suppressed RANKL-stimulated osteoclastogenesis and the bone resorption activity of mature osteoclasts. **(A)** Drugs or different nanoparticles continued to interfere BMMs differentiation induced by RANKL (100ng/mL) for 7 days, mature osteoclasts were labeled purplish red, and cells with nuclei greater than or equal to 3 were counted to calculate the proportion of TRAP positive multinucleated cells. Scale bar = 100µm. **(B)** BMMs were incubated with RANKL (100ng/mL) plus drugs or different nanoparticles for 7 days. F-actin rings were observed by phalloidin staining, and the percentage of the total area was calculated. Scale bar = 100µm. **(C)** BMMs were incubated with RANKL (100ng/mL) plus drugs or different nanoparticles on the slice of bovine cortex bone for 7 days. The slice appearance was recorded by SEM, and the percentage of resorbed area was calculated. Scale bar = 200µm. * $p < 0.05$; ** $p < 0.01$; *** $p < 0.001$ compared to the control group. # $p < 0.05$ compared to the MSNs-Naringin group.

Abbreviations: MSNs-Nar, MSNs-Naringin; CS@MSNs-Nar, CS@MSNs-Naringin.

Mature osteoclasts secrete H^+ , Cl^- , and Cathepsin K in closed acidic resorption lacunae to degrade bone tissue, counteracting osteoblast-induced osteogenesis.³² Inducing osteoclast resorption in bovine cortical bone slices revealed that Naringin and MSNs-Naringin inhibited the bone resorption capacity of osteoclasts to some extent, while CS@MSNs-Naringin almost completely abolished osteoclast resorption (Figure 3C).

Osteoclast differentiation, induced by Receptor Activator of Nuclear Factor Kappa-B Ligand (RANKL) and Macrophage Colony-Stimulating Factor (M-CSF), involves multiple stages, including osteoclast precursor cells, non-functional polykaryons, and mature osteoclasts.³² Therefore, exploring the specific stage where CS@MSNs-Naringin inhibits osteoclast formation is significant. In the 7-day differentiation process of osteoclasts, we divided the intervention into three periods and found that the introduction of CS@MSNs-Naringin in the early stage exhibited the most potent inhibitory impact on osteoclast formation, followed by its introduction during the middle stage. In contrast, when introduced late, it yielded the weakest inhibitory effect, suggesting that CS@MSNs-Naringin primarily impedes osteoclastogenesis during its early stages (Supplementary Figure 3A).

Effect of CS@MSNs-Naringin on Characteristic mRNA Expression During Osteoclast Formation Induced by RANKL

After RANKL stimulation, c-Fos is induced to form activating protein-1 (AP-1), which is recruited to the promoter region of the NFATc1 gene, resulting in the nuclear translocation of NFATc1. This transcription factor subsequently regulates the expression of various osteoclast genes, including TRAP, Cathepsin K, and DC-STAMP. All these genes are essential for osteoclast formation and function. Naringin, MSNs-Naringin, and CS@MSNs-Naringin significantly inhibited the mRNA expression of c-Fos, reducing the recruitment of the NFATc1 gene. As a result, the expression of DC-STAMP, Cathepsin K, and TRAP, all essential for osteoclast function, was reduced (Figure 4A). Moreover, CS@MSNs-Naringin exhibited a stronger inhibitory effect than MSNs-Naringin for c-Fos, NFATc1, DC-STAMP, and Cathepsin K (Figure 4A).

Effect of CS@MSNs-Naringin on MAPK and NF- κ B Signaling Pathways of Osteoclast

It has been reported that the RANKL and RANK interaction activates the NF- κ B and MAPK signaling pathways in osteoclasts.² These pathways are crucial for osteoclast differentiation and function. CS@MSNs-Naringin significantly inhibited the phosphorylation of p38, ERK, and JNK in the MAPK pathway. MSNs-Naringin significantly inhibited p38 and ERK, while Naringin mainly inhibited ERK phosphorylation (Figure 4B). In the NF- κ B signaling pathway, both MSNs-Naringin and CS@MSNs-Naringin inhibited the phosphorylation of I κ B α and NF- κ B, with CS@MSNs-Naringin exhibiting a more pronounced inhibitory effect. Importantly, CS@MSNs-Naringin also inhibited the degradation of I κ B α . In contrast, Naringin alone did not significantly affect the NF- κ B signaling pathway (Figure 4B). Moreover, CS@MSNs-Naringin exhibited significant inhibition of c-Fos and NFATc1, which are downstream proteins in the MAPK and NF- κ B signaling pathways. MSNs-Naringin only effectively inhibited c-Fos protein expression (Figure 4B).

To further confirm these results, the translocation of NFATc1 to the nucleus was observed through immunofluorescence. Both CS@MSNs-Naringin, MSNs-Naringin, and Naringin reduced the fluorescence intensity of NFATc1 in the nucleus, with CS@MSNs-Naringin showing a stronger effect (Figure 5).

Effect of CS@MSNs-Naringin on Apoptosis of Osteoclasts

Previous research showed that Naringin could promote mitochondrial apoptosis in osteoclasts. The present study examined the regulation of osteoclast apoptosis by CS@MSNs-Naringin. CS@MSNs-Naringin exhibited the most effective promotion of osteoclast apoptosis compared to Naringin and MSNs-Naringin, increasing the expression of pro-apoptotic proteins Bax and Cleaved-caspase 3 while inhibiting the anti-apoptotic protein Bcl-2 (Figure 6A). To further confirm these results, TUNEL staining was used to evaluate nuclear DNA breakdown during apoptosis. Both MSNs-Naringin and CS@MSNs-Naringin promoted early apoptosis of osteoclasts, with CS@MSNs-Naringin yielding the most pronounced effect (Figure 6B).

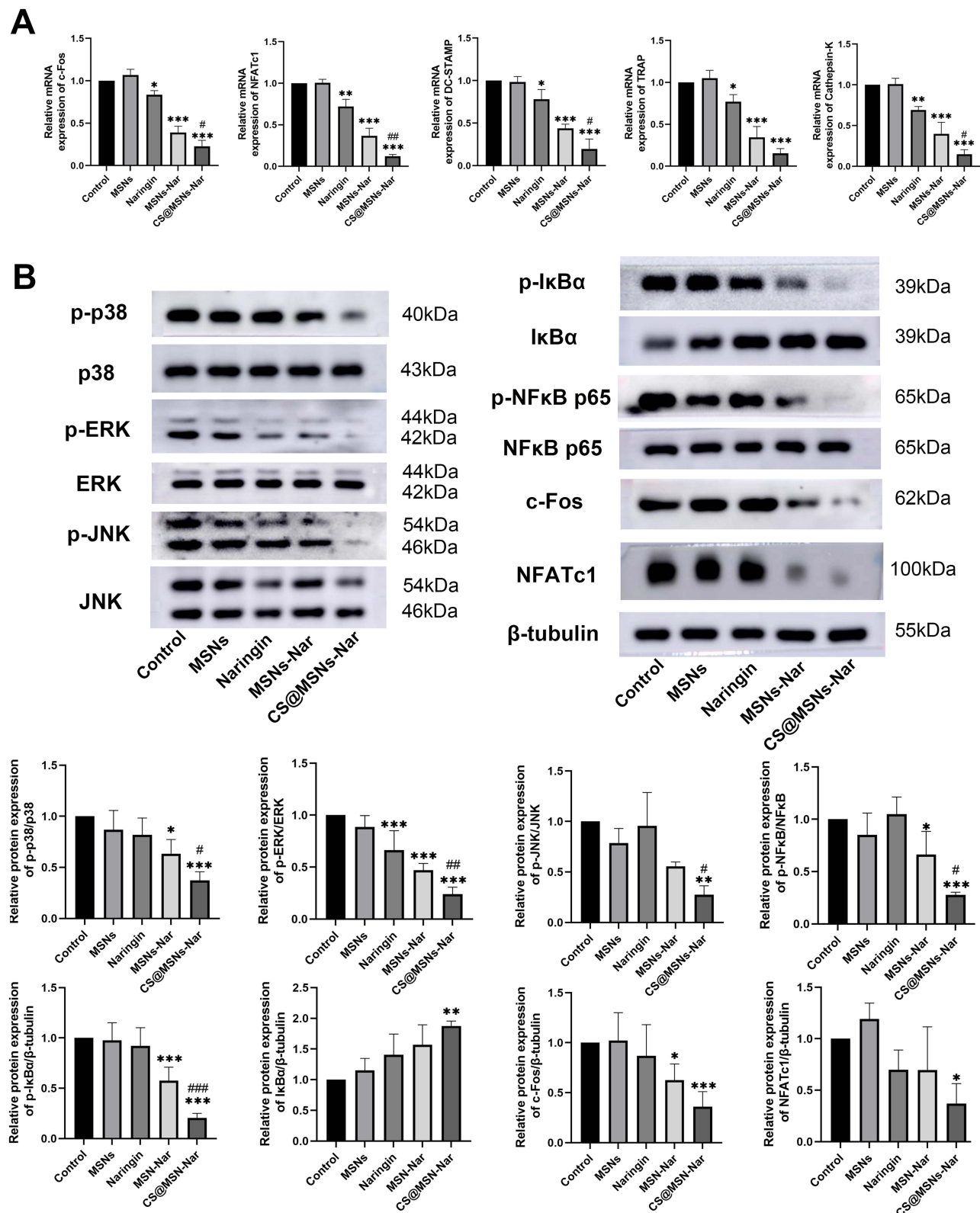


Figure 4 CS@MSNs-Naringin suppressed the mRNA and protein expression levels of osteoclast-related genes and signal channels. **(A)** BMMs were incubated with RANKL (100ng/mL) plus drugs or different nanoparticles for 7 days. Expression levels of osteoclast-related mRNA compared with GAPDH. **(B)** Expression levels of key proteins in MAPK and NFκB signaling pathways by Western blotting. * $p < 0.05$; ** $p < 0.01$; *** $p < 0.001$ compared to the control group. # $p < 0.05$, ## $p < 0.01$, ### $p < 0.001$ compared to the MSNs-Naringin group.

Abbreviations: MSNs-Nar, MSNs-Naringin; CS@MSNs-Nar, CS@MSNs-Naringin.

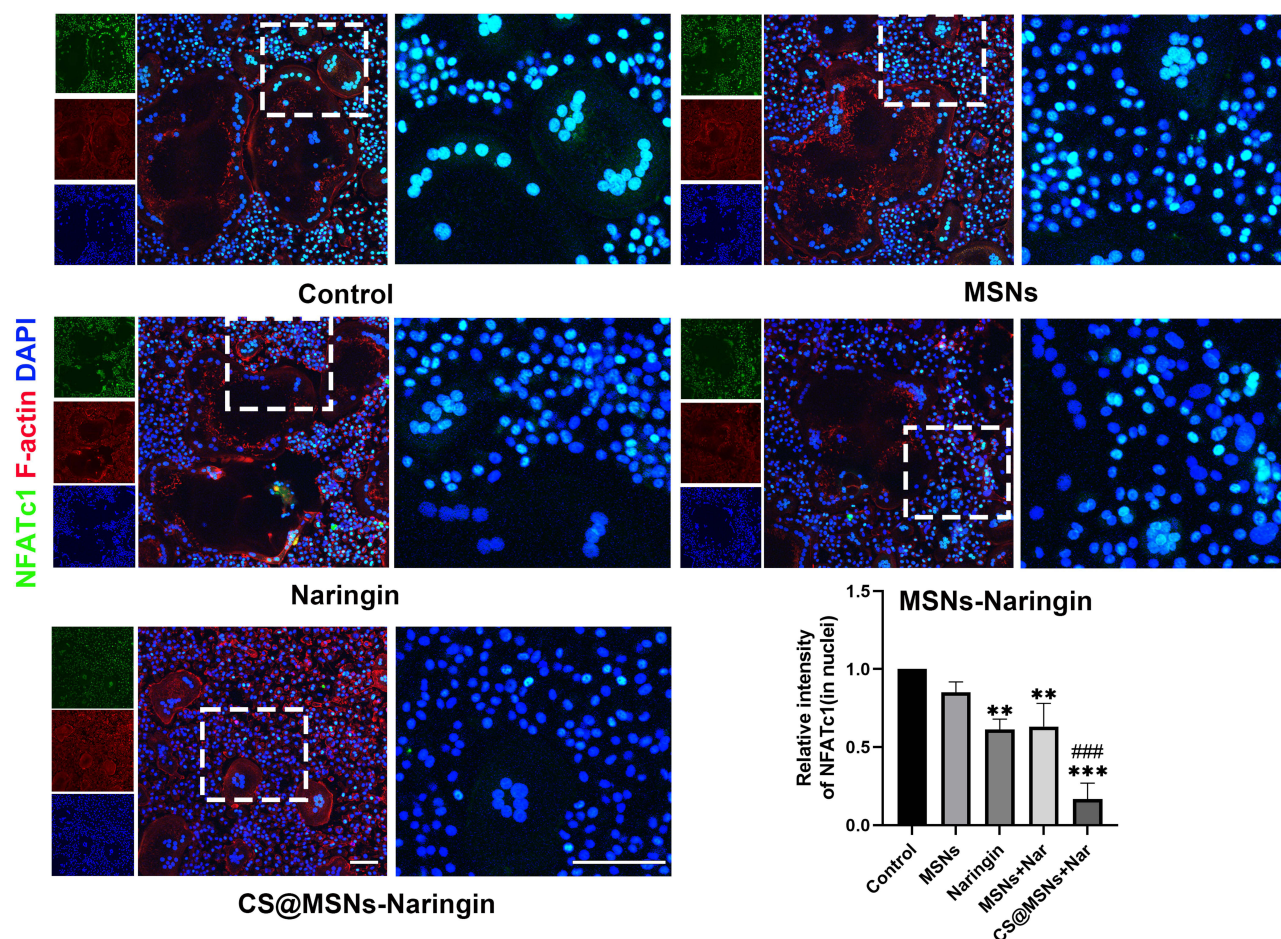


Figure 5 CS@MSNs-Naringin inhibited the nuclear translocation of NFATc1. BMMs were incubated with RANKL (100ng/mL) plus drugs or different nanoparticles for 7 days. NFATc1 is labeled green, F-actin red, and the nucleus blue. The fluorescence intensity of NFATc1 in the nucleus was quantified in terms of mean and standard deviation (n=3). ** $p < 0.01$; *** $p < 0.001$ compared to the control group. #### $p < 0.001$ compared to the MSNs-Naringin group. Scale bar=100 μ m.

Abbreviations: MSNs-Nar, MSNs-Naringin; CS@MSNs-Nar, CS@MSNs-Naringin.

Characterization of GelMA Hydrogels

In this section, we designed GelMA hydrogels incorporating nanoparticles to enable the in situ release of nanoparticles within bone defects. We prepared various hydrogels: GelMA, GelMA+Naringin, GelMA+MSNs, GelMA+MSNs-Naringin, and GelMA+CS@MSNs-Naringin hydrogels (as shown in Figure 7A). To assess the degradation of these hydrogels, we immersed GelMA, GelMA+Naringin, GelMA+MSNs, GelMA+MSNs-Naringin, and GelMA+CS@MSNs-Naringin hydrogels in PBS at 37°C and recorded the remaining mass at different time points. At day 28, the degradation rates were 33.53% \pm 1.81 for group GelMA, 32.07% \pm 1.87 for group GelMA+MSNs, 32.42% \pm 2.49 for group GelMA+Naringin, 31.96% \pm 1.06 for group GelMA+MSNs-Naringin, 31.96% \pm 1.06 for group GelMA+MSNs-Naringin, and 29.23% \pm 1.50 for group GelMA+CS@MSNs-Naringin. In contrast, the degradation rates of each group were not statistically significant, indicating that the addition of nanomaterials in each group did not affect the degradation of GelMA hydrogel (Figure 7B). Notably, the mechanical properties of these GelMA hydrogels were examined since both excessive stiffness and low strength can adversely affect implant stability and surrounding bone tissue integrity. As shown in Figure 7C, At the same 0.5% strain, the stress of GelMA is 5.40mPa, while the stress of GelMA+MSNs-Naringin is increased to 8.92mPa. The stiffness of GelMA increased with the addition of CS@MSNs-Naringin. Additionally, the swelling rate of hydrogels, which reflects their water absorption capacity, was evaluated. Excessive swelling can increase intracranial pressure in the rat calvarial bone defect model, potentially causing cerebral hernias. Importantly, GelMA+MSNs (4.39 \pm 0.35), GelMA+MSNs-Naringin (4.23 \pm 0.37),

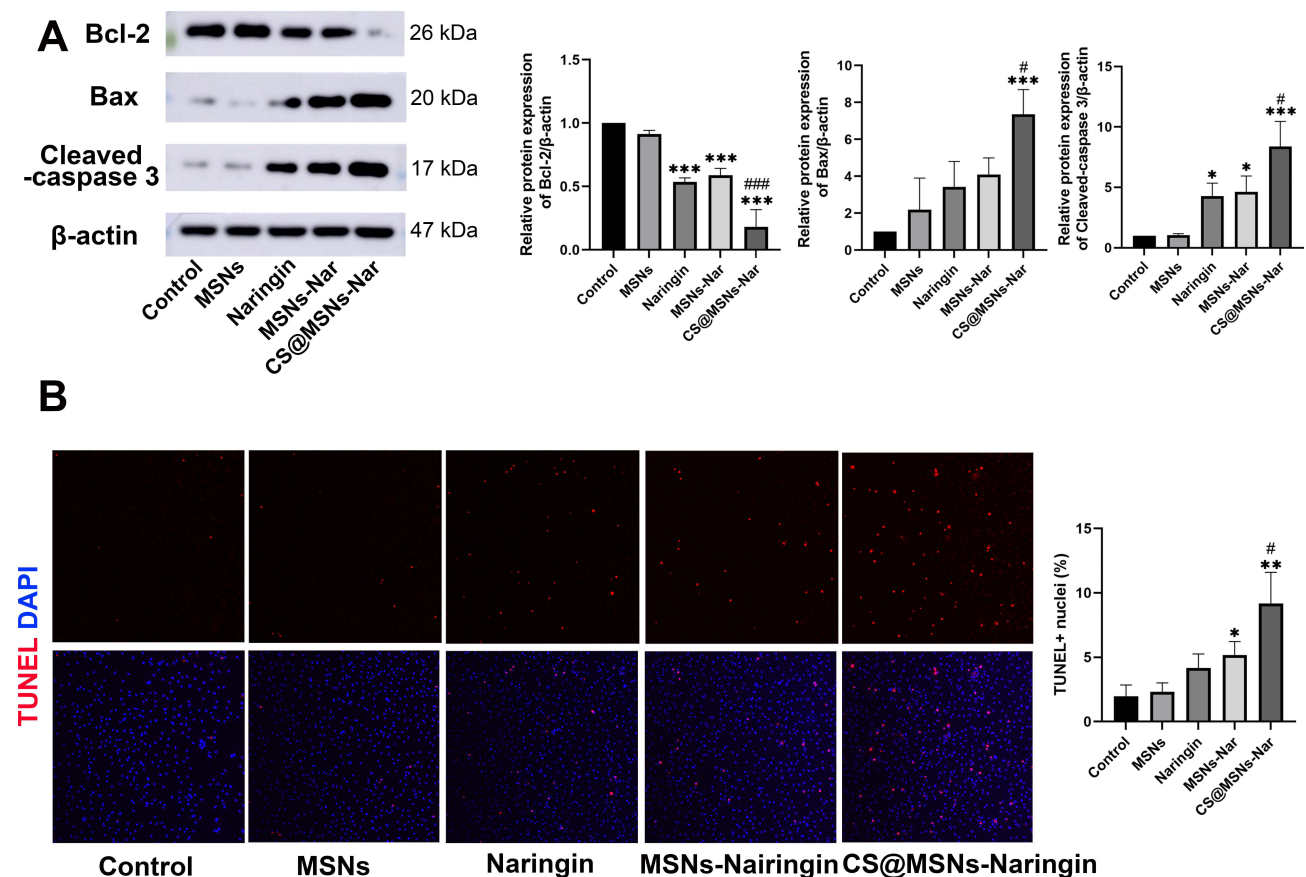


Figure 6 CS@MSNs-Naringin promoted the apoptosis of osteoclasts and progenitors. **(A)** The expression of apoptosis-related proteins (Bcl-2, Bax, Cleaved-caspase 3) compared with β-actin by Western blotting. **(B)** BMMs were incubated with RANKL (100ng/mL) plus drugs or different nanoparticles for 7 days. TUNEL positive cells are marked red, and the percentage of positive cells was calculated. * $p < 0.05$; ** $p < 0.01$; *** $p < 0.001$ compared to the control group. # $p < 0.05$, ## $p < 0.01$, ### $p < 0.001$ compared to the MSNs-Naringin group. Scale bar=100μm.

Abbreviations: MSNs-Nar, MSNs-Naringin; CS@MSNs-Nar, CS@MSNs-Naringin.

and GelMA+CS@MSNs-Naringin (3.17 ± 0.22) hydrogels could reduce the swelling ratio of GelMA (5.97 ± 0.22) (Figure 7D).

One key feature of GelMA is its ability to solidify into different shapes upon exposure to ultraviolet light. Interestingly, the addition of CS@MSNs-Naringin did not impact the shape plasticity of GelMA, as demonstrated in Figure 7Ea and b. For successful utilization as a carrier for nanomaterials, it is essential for GelMA to maintain a large, interconnected pore structure that supports cell infiltration and nutrient exchange. In this context, both GelMA and GelMA+CS@MSNs-Naringin hydrogels exhibited a similar spongy porous structure, confirming that the inclusion of CS@MSNs-Naringin did not compromise the porous structure of GelMA hydrogels. Furthermore, although the section surface of the GelMA+CS@MSNs-Naringin composite hydrogel appeared rougher in comparison to plain GelMA, no nanoparticle clusters were present in the magnified image, demonstrating efficient nanoparticle dispersion within the hydrogel (Figure 7F). Si elemental mapping similarly confirmed the successful loading of CS@MSNs-Naringin in GelMA and the uniform dispersion in the gel (Supplementary Figure 4A).

The drug release experiment showed that with the degradation of GelMA hydrogel induced by collagenase II, naringin was released continuously at a stable rate, and the cumulative release rate reached 75.23% on the 20th day (Supplementary Figure 4B).

Evaluation of Biosafety of Implant in vivo

In a two-month rat calvarial bone defect model, GelMA, with or without naringin and nanoparticles, was used to fill the defects and ensure controlled in situ release. Subsequently, the rats were euthanized, and major metabolic organs (the

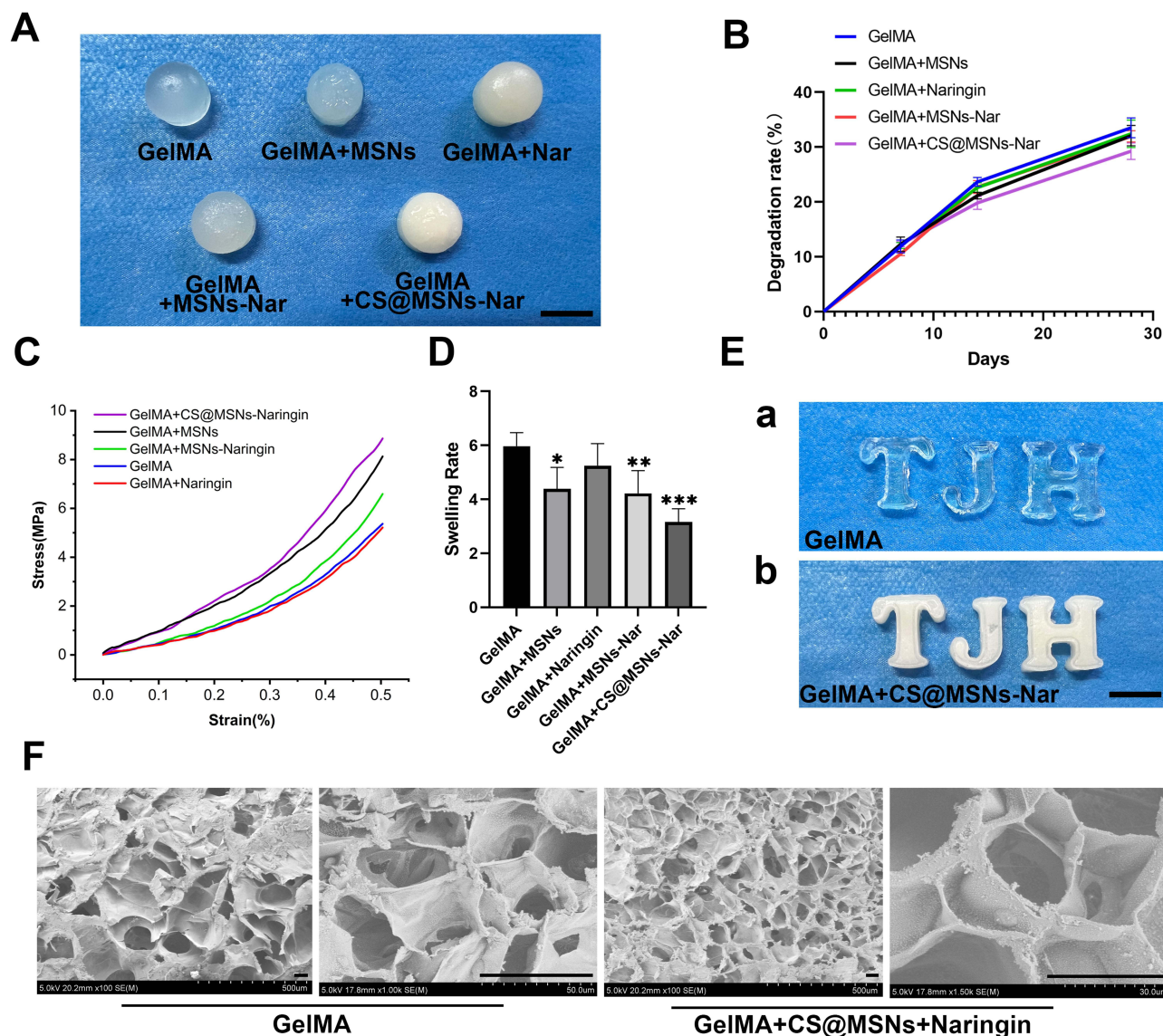


Figure 7 The characteristics of the GelMA hydrogel. **(A)** Photograph of different GelMA hydrogels. Scale bar=500mm. **(B)** The degradation rate of different GelMA hydrogels at 7, 14, and 21 days. **(C)** The stress-strain curve of different GelMA hydrogel. **(D)** The swelling rate of different GelMA hydrogels ($n=3$). *: $p<0.05$; **: $p<0.01$; ***: $p<0.001$ compared to the GelMA group. **(E)** The shape plasticity of GelMA and GelMA+CS@MSNs-Naringin hydrogel. (a) GelMA, (b) GelMA with CS@MSNs-Naringin. Scale bar=1cm. **(F)** SEM scanning of hydrogel section of GelMA and GelMA+CS@MSNs-Naringin. Scale bar=50µm.

brain, heart, liver, spleen, lung, and kidney) were extracted. Importantly, no significant pathological changes were detected in major organs when subjected to HE staining, irrespective of the experimental group, including the Control group, GelMA group, Naringin group, MSNs group, MSNs-Naringin group, or CS@MSNs-Naringin group (Supplementary Figure 3B).

Micro-CT Measurements

After two months of implantation, adding Naringin, MSNs-Naringin, and CS@MSNs-Naringin led to a partial increase in new bone formation within the bone defects compared to the Control and GelMA groups. Notably, in the Naringin group, new bone formation was primarily limited to the defect's periphery, with minimal new bone observed in the center. Conversely, in the MSNs-Naringin and CS@MSNs-Naringin groups, new bone extended more prominently toward the center of the defect (Figure 8A). Specifically, CS@MSNs-Naringin significantly improved parameters such as BV/TV ($0.49\%\pm 0.03$), Tb.N (2.03

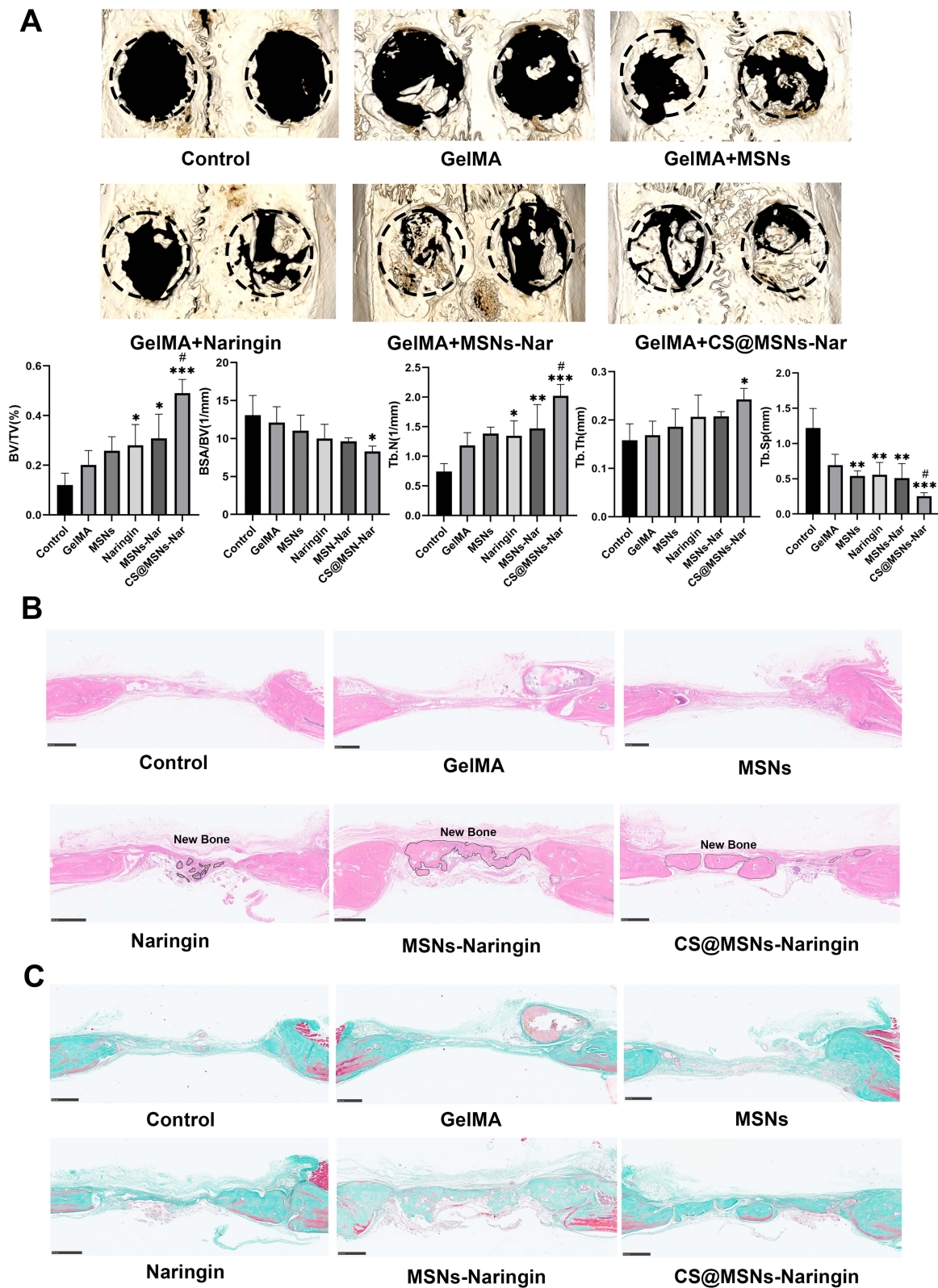


Figure 8 Imaging and histomorphological analysis of calvarial bone in rats with bone defect. **(A)** 3D reconstruction images of Micro-CT, and the bone volume/total volume (BV/TV), bone surface area/bone volume (BSA/BV), trabecular separation (Tb.Sp), trabecular number (Tb.N), and trabecular thickness (Tb.Th) were analyzed (n=3). * $p < 0.05$; ** $p < 0.01$, *** $p < 0.001$ compared to the control group. # $p < 0.05$ compared to the MSNs-Naringin group. **(B)** and **(C)** HE and Goldner staining of calvarial bone in rats with bone defect. Scale bar=500 μ m.

1/mm \pm 0.09), and Tb.Th (0.24 mm \pm 0.01), while reducing BAS/BV (8.29 1/mm \pm 0.36) and Tb.Sp (0.25mm \pm 0.02). It is worth noting that CS@MSNs-Naringin yields a better effect than MSNs-Naringin in regulating BV/TV, Tb.N, and Tb.Sp (Figure 8A).

Histological Observations and Histomorphometric Analysis

Histological images obtained from Goldner trichromatic and HE staining are presented in Figure 8B and C. Notably, the bone defects in the Control, GelMA, and MSNs groups were predominantly filled with fibrous connective tissue, lacking significant new bone formation. In contrast, the Naringin group displayed limited new bone formation within the defect. In the MSNs-Naringin and CS@MSNs-Naringin groups, many new bone islands and mature new bone were observed,

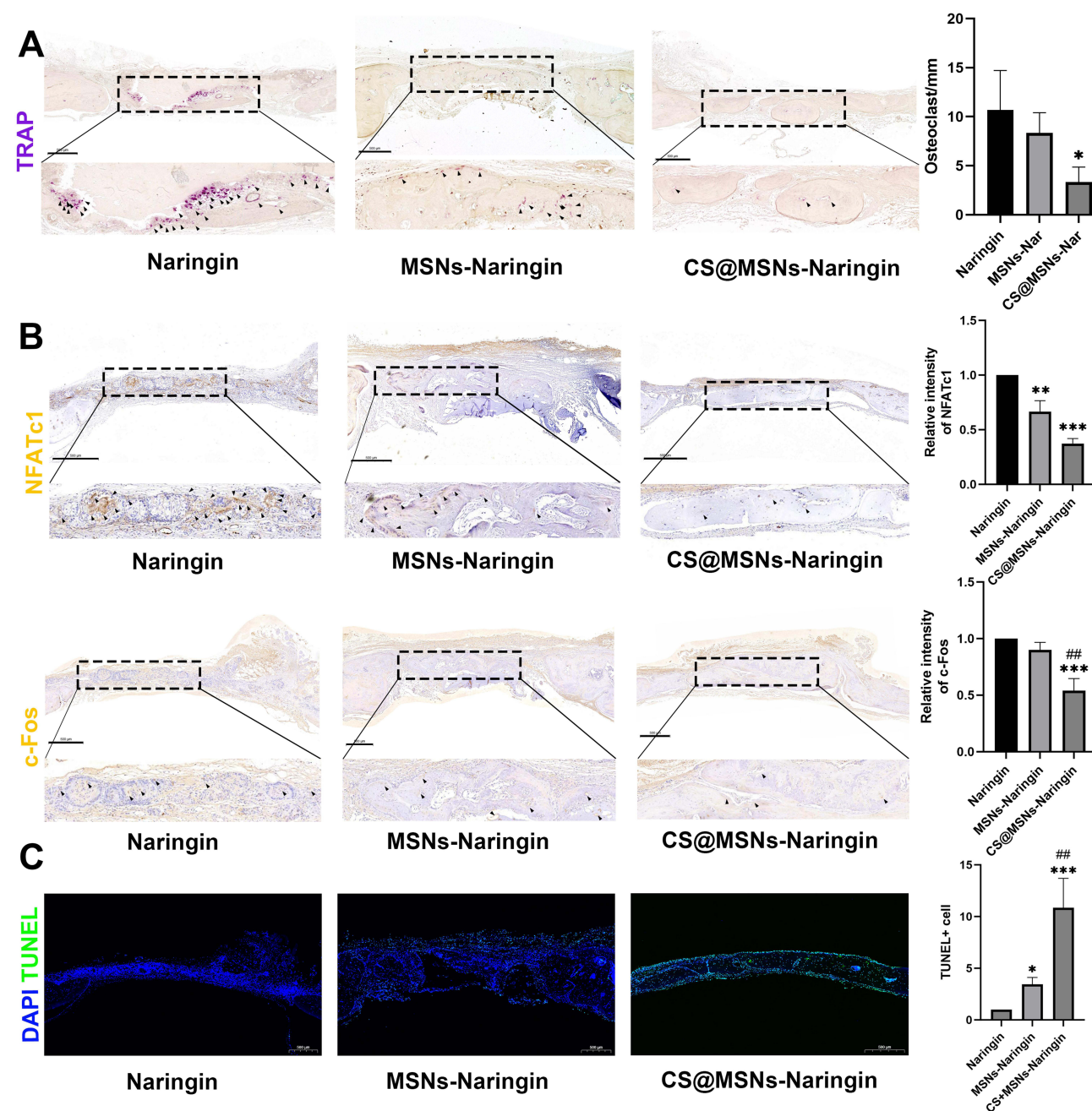


Figure 9 CS@MSNs-Naringin inhibits osteoclasts in vivo. **(A)** TRAP staining of calvarial bone in rats with bone defect. TRAP-positive cells are labeled purple and indicated by a black arrow. **(B)** Representative immunohistochemical images of NFATc1 and c-Fos expression. Positive cells are labeled brownish-yellow and indicated by a black arrow. * p <0.05; ** p <0.01; *** p <0.001 compared to the Naringin group. ## p <0.01 compared to the MSN-Naringin group. **(C)** The TUNEL staining images of Naringin, MSNs-Naringin, CS@MSNs-Naringin. * p <0.05; *** p <0.001 compared to the Naringin group. ## p <0.01 compared to the MSN-Naringin group.

accompanied by a substantial presence of osteoblasts and osteocytes. Importantly, the new bone volume and connectivity density were superior in the CS@MSNs-Naringin group compared to the MSNs-Naringin group (Figure 8B and C).

TRAP staining revealed a few osteoclasts within the new bone tissue of the Naringin, MSNs-Naringin, and CS@MSNs-Naringin groups (Figure 9A). Additionally, the quantification of TRAP-positive cells confirmed that the number of these cells in the CS@MSNs-Naringin group was significantly lower than in the Naringin and MSNs-Naringin groups, supporting the results obtained from *in vitro* experiments (Figures 9A).

Immunohistochemical staining targeting NFATc1 and c-Fos corroborated the TRAP staining results, indicating that the expression of NFATc1 and c-Fos was notably lower in the CS@MSNs-Naringin group, followed by the MSNs-Naringin group and the Naringin group (Figures 9B).

TUNEL staining of rat skull sections confirmed the ability of CS@MSNs-Naringin to promote osteoclast and precursor cell apoptosis observed *in vitro*. Compared with MSNs-Naringin, CS@MSNs-Naringin exhibits a stronger ability to promote the apoptosis of osteoclasts and precursor cells in the new bone (Figures 9C).

Discussion

In this study, we successfully prepared acid-sensitive gated CS@MSNs-Naringin and observed its potential to inhibit osteoclast production and bone resorption capacity. This inhibitory effect was associated with attenuated MAPK and NF- κ B signaling pathways, a reduction in the expression of genes associated with osteoclasts, including TRAP, c-fos, NFATc1, Cathepsin-K, and DC-STAMP, and the promotion of osteoclast apoptosis *in vitro*. Moreover, *in vivo* experiments demonstrated that CS@MSNs-Naringin, when contained in GelMA, promoted bone regeneration while decreasing osteoclast activity.

Environmentally intelligent responsive nanoparticles can react to environmental pH, reactive oxygen species, strain, electricity, light, etc.³³ The choice of pH-sensitive nanoparticles for drug delivery in our study was due to the unique acid dependence of osteoclasts. Osteoclasts are unique cells that differentiate from monocyte/macrophage lineage cells and are primarily responsible for bone resorption.³² Recent research into the connection between osteoclasts and protons has made some advancements. During osteoclast differentiation, metabolic reprogramming is crucial in maintaining energy supply. This accelerates glycolysis and oxidative phosphorylation, increasing ATP and lactic acid production.^{5,6} Furthermore, mature osteoclasts require high energy metabolism as they carry out bone resorption, necessitating substantial ATP for actin and cytoskeleton rearrangement. This cellular activity also generates lactic acid as a by-product.⁵ As osteoclasts dissolve the bone matrix, they create a resorption lacuna between the osteoclast and the bone surface. In this space, osteoclasts release protons and enzymes, primarily Cathepsin K, to dissolve bone.² The resorption lacuna is acidified due to the release of protons, and this acidification is efficient, reducing the pH to 3 within a few minutes of the resorption space.⁷ Moreover, the excess protons return to the cytoplasm, causing periodic pH oscillations within osteoclasts.⁷ This pH dynamic has raised questions regarding whether the cytoplasm becomes alkalized during the proton release into the resorption lacuna. Recent mathematical models suggest that AE2 plays a role in preventing alkalization within osteoclasts, even in the face of substantial proton release.³⁴ Furthermore, organelles within osteoclasts, such as endosomes (pH: 4.9–6.0)⁸ and lysosomes (pH: 4.0–4.5),⁹ have a lower pH than the standard cellular environment. Notably, these organelles are responsible for the internalization of nanoparticles by osteoclasts.³⁵ Based on the above relationship between the physiological characteristics of osteoclasts and microenvironment pH, most current studies inhibit osteoclasts by macroscopically regulating the pH in the bone microenvironment. For example, borosilicate can effectively weaken the proton concentration in the microenvironment, and a weakly alkaline microenvironment can inhibit abnormally activated osteoclasts to promote the regeneration of osteoporotic bone.³⁶ Studies aimed at producing pH-sensitive osteoclast intracellular internalizing nanomaterials are rare, which is the novel aspect of this research.

We first prepared CS@MSNs-Naringin nanoparticles. The particle size selection of nanomaterials is crucial, and nanoparticles with a particle size less than 10 nm can be rapidly eliminated by the kidney. However, nanoparticles larger than 200 nm activate the complement system and are rapidly cleared from the bloodstream.³⁷ In this study, the particle size of the fabricated nanomaterials was in the range of 100–150nm, which met the experimental requirements. Besides, safety is a paramount consideration and prerequisite for the clinical application of nanomaterials. While MSNs present remarkable advantages and hold great promise for medical applications, with instances of their use in human trials (NCT02106598),³⁸ their potential biotoxicity must be rigorously assessed. Our study found that MSNs are safe for bone

marrow-derived macrophages (BMMs) and MC3T3-E1 cells, representing the skeletal system, at 80 µg/mL or lower concentrations, consistent with the literature.^{39–41} Danial et al suggested that MSNs are safe for cells below 100 µg/mL, at this concentration, MSNs can be excreted in the urine.⁴⁰ At the molecular level, the siloxane skeleton of MSNs undergoes hydrolysis in vivo, producing non-toxic byproducts such as orthosilicic acid and polysilicic acid, eventually eliminated.^{41,42} This assures MSNs' good biocompatibility and minimal bioaccumulation. Surprisingly, the biosafety of CS@MSNs-Naringin was even higher after chitosan modification, with a maximum safe dose of 120 µg/mL. This phenomenon can be attributed to chitosan's greater biocompatibility compared to mesoporous silica.⁴³ Subsequently, our in vivo experiments confirmed the biosafety of CS@MSNs-Naringin, with no evidence of toxicity to major metabolic organs. The biological safety of chitosan is recognized by the current research. For example, the study of Abou-Saleh et al showed that chitosan nanoparticles did not exhibit obvious toxic and teratogenic phenotypes at concentrations up to 200 mg/L.⁴⁴ This is consistent with the results of the present study.

To assess the effect of CS@MSNs-Naringin on osteoclast biology, CS@MSNs-Naringin was uniformly dispersed in α -MEM through ultrasound. Recent studies have shown internalized MSNs can still be observed within cells using confocal microscopy after seven days, suggesting that cells do not excrete nanoparticles during this period.^{45,46} This feature offers an advantage in terms of reducing the frequency and dose of administration, thus minimizing the potential for adverse drug reactions. This is the reason why the culture medium containing different nanoparticles and drugs was used only in the first intervention in this study. This can also explain why our previous study confirmed that naringin has the function of inhibiting osteoclasts, but naringin lost the above inhibitory effect in some sections of this study. This is because in the previous study, Naringin was continuously added with each replacement of culture medium. In this study, CS@MSNs-Naringin and MSNs-Naringin could continuously release naringin, while the naringin group lost its dosing advantage. In vitro, CS@MSNs-Naringin inhibited osteoclast formation and activity through MAPK and NF κ B signaling pathways. Notably, NFATc1, the master transcription factor in osteoclast formation, is crucial for osteoclast function. Previous studies confirmed that NFATc1 deficiency resulted in complete loss of osteoclastic bone resorptive activity.⁴⁷ We confirmed that CS@MSNs-Naringin inhibits NFATc1 expression and nuclear translocation in several ways.

Repairing bone defects presents a significant clinical challenge, impacting the aesthetics and quality of life for patients and placing a substantial burden on society. In recent years, significant strides have been made in the research of biomaterials to promote bone regeneration. However, it should be acknowledged that osteoclasts play a crucial role in bone regeneration.⁴⁸ To evaluate the role of CS@MSNs-Naringin in addressing calvarial bone defects, GelMA hydrogel, a biologically compatible scaffold, was utilized to conform to the defect's shape under ultraviolet light and facilitate the in-situ delivery of CS@MSNs-Naringin. Notably, GelMA hydrogel is suitable for shaping amorphous defects and can precisely fill them. Furthermore, GelMA's structure remains stable for an extended period, and its degradation rate can be controlled through varying proportions.⁴⁹ By incorporating stem cell-derived vesicles, it has been effectively employed in cartilage defect regeneration.⁴⁹ Our research demonstrated that, compared to Naringin and MSNs-Naringin, CS@MSNs-Naringin significantly promotes new bone formation. Importantly, this effect is accompanied by the suppression of osteoclast activity and a reduction in the expression of NFATc1 and c-Fos. Taken together, these findings suggest that CS@MSNs-Naringin may represent a promising therapeutic strategy for addressing bone defects by targeting osteoclasts.

Conclusions

In summary, CS@MSNs-Naringin, a pH-sensitive gated nano-drug delivery system, displayed remarkable potential in inhibiting osteoclast generation, bone resorption activity, and promotion of apoptosis, with concurrent inhibition of the MAPK and NF- κ B signaling pathways, ultimately reducing the expression of osteoclast-specific genes and proteins in vitro. Furthermore, in an in vivo setting, CS@MSNs-Naringin effectively promoted bone regeneration in calvarial bone defects while reducing osteoclast formation. The limitation of this study is that it only focused on the functional regulation of drug-loaded nanoparticles on osteoclasts. Indeed, bone mass is co-regulated by subtle crosstalk between osteoblasts and osteoclasts. This is the future direction of this study.

Acknowledgments

We thank Home for Researchers editorial team (www.home-for-researchers.com) for language editing service.

Funding

This work was supported by a grant from National Natural Science Foundation of China (No. 81871777, 81572154, 11772226, 82304976), Tianjin Science and Technology Plan Project (No. 18PTLCSY00070, 16ZXZNGX00130), Tianjin Science and Technology Plan Key Project (No. 22JCZDJC00340), National Key Research and Development Plan (No. 2022YFC3601900).

Disclosure

The authors report no conflicts of interest in this work.

References

- Kim JM, Lin C, Stavre Z, Greenblatt MB, Shim JH. Osteoblast-osteoclast communication and bone homeostasis. *Cells*. 2020;9(9):2073. doi:10.3390/cells9092073
- Udagawa N, Koide M, Nakamura M, et al. Osteoclast differentiation by RANKL and OPG signaling pathways. *J Bone Miner Metab*. 2021;39(1):19–26. doi:10.1007/s00774-020-01162-6
- Jacome-Galarza CE, Percin GI, Muller JT, et al. Developmental origin, functional maintenance and genetic rescue of osteoclasts. *Nature*. 2019;568(7753):541–545. doi:10.1038/s41586-019-1105-7
- Guo YF, Su T, Yang M, et al. The role of autophagy in bone homeostasis. *J Cell Physiol*. 2021;236(6):4152–4173. doi:10.1002/jcp.30111
- Da W, Tao L, Zhu Y. The Role of osteoclast energy metabolism in the occurrence and development of osteoporosis. *Front Endocrin*. 2021;12:675385. doi:10.3389/fendo.2021.675385
- Kim JM, Jeong D, Kang HK, Jung SY, Kang SS, Min BM. Osteoclast precursors display dynamic metabolic shifts toward accelerated glucose metabolism at an early stage of RANKL-stimulated osteoclast differentiation. *Cell Physiol Biochem*. 2007;20(6):935–946. doi:10.1159/000110454
- Gong S, Ma J, Tian A, Lang S, Luo Z, Ma X. Effects and mechanisms of microenvironmental acidosis on osteoclast biology. *Biosci Trends*. 2022;16(1):58–72. doi:10.5582/bst.2021.01357
- Huotari J, Helenius A. Endosome maturation. *EMBO J*. 2011;30(17):3481–3500. doi:10.1038/emboj.2011.286
- Wang C, Zhao T, Li Y, Huang G, White MA, Gao J. Investigation of endosome and lysosome biology by ultra pH-sensitive nanopores. *Adv Drug Deliv Rev*. 2017;113:87–96. doi:10.1016/j.addr.2016.08.014
- The North American Menopause Society. Management of osteoporosis in postmenopausal women: the 2021 position statement of the north American menopause society. *Menopause*. 2021;28(9):973–997. doi:10.1097/GME.0000000000001831
- Kanis JA, Cooper C, Rizzoli R, Reginster JY. Scientific Advisory Board of the European Society for Clinical and Economic Aspects of Osteoporosis (ESCEO), the Committees of Scientific Advisors and National Societies of the International Osteoporosis Foundation (IOF). European guidance for the diagnosis and management of osteoporosis in postmenopausal women. *Osteoporos Int*. 2019;30(1):3–44. doi:10.1007/s00198-018-4704-5
- Kim HS, Suh KS, Sul D, Kim BJ, Lee SK, Jung WW. The inhibitory effect and the molecular mechanism of glabridin on RANKL-induced osteoclastogenesis in RAW264.7 cells. *Int J Mol Med*. 2012;29(2):169–177. doi:10.3892/ijmm.2011.822
- Park SH, Kim JY, Cheon YH, et al. Protocatechuic acid attenuates osteoclastogenesis by downregulating JNK/c-Fos/NFATc1 signaling and prevents inflammatory bone loss in mice. *Phytother Res*. 2016;30(4):604–612. doi:10.1002/ptr.5565
- Zhang Q, Tang X, Liu Z, et al. Hesperetin prevents bone resorption by inhibiting rankl-induced osteoclastogenesis and Jnk Mediated Irf-3/c-Jun Activation. *Front Pharmacol*. 2018;9:1028. doi:10.3389/fphar.2018.01028
- Huh JE, Jung IT, Choi J, et al. The natural flavonoid galangin inhibits osteoclastic bone destruction and osteoclastogenesis by suppressing NF-κB in collagen-induced arthritis and bone marrow-derived macrophages. *Eur J Pharmacol*. 2013;698(1–3):57–66. doi:10.1016/j.ejphar.2012.08.013
- Kim JY, Lee MS, Baek JM, Park J, Youn BS, Oh J. Massive elimination of multinucleated osteoclasts by eupatilin is due to dual inhibition of transcription and cytoskeletal rearrangement. *Bone Rep*. 2015;3:83–94. doi:10.1016/j.bonr.2015.10.003
- Alam MA, Subhan N, Rahman MM, Uddin SJ, Reza HM, Sarker SD. Effect of citrus flavonoids, naringin and naringenin, on metabolic syndrome and their mechanisms of action. *Adv Nutr*. 2014;5(4):404–417. doi:10.3945/an.113.005603
- Ramesh P, Jagadeesan R, Sekaran S, Dhanasekaran A, Vimalraj S. Flavonoids: Classification, function, and molecular mechanisms involved in bone remodelling. *Front Endocrinol*. 2021;12:779638. doi:10.3389/fendo.2021.779638
- Ma X, Lv J, Sun X, Ma J, Xing G, Wang Y. Naringin ameliorates bone loss induced by sciatic neurectomy and increases Semaphorin 3A expression in denervated bone. *Sci Rep*. 2016;6:24562. doi:10.1038/srep24562
- Li F, Sun X, Ma J, Ma X, Zhao B, Zhang Y. Naringin prevents ovariectomy-induced osteoporosis and promotes osteoclasts apoptosis through the mitochondria-mediated apoptosis pathway. *Biochem Biophys Res Com*. 2014;452(3):629–635. doi:10.1016/j.bbrc.2014.08.117
- Zhang J, Zhuang Y, Sheng R, et al. Smart stimuli-responsive strategies for titanium implant functionalization in bone regeneration and therapeutics. *Mater Horiz*. 2024;11(1):12–36. doi:10.1039/d3mh01260c
- Cui Y, Hong S, Jiang W, et al. Engineering mesoporous bioactive glasses for emerging stimuli-responsive drug delivery and theranostic applications. *Bioact Mater*. 2024;34:436–462. doi:10.1016/j.bioactmat.2024.01.001
- Wang Y, Yang Y, Wu T, et al. Dendritic porous silica nanoparticles with high-curvature structures for a dual-mode DNA sensor based on fluorometer and person glucose meter. *Mikrochim Acta*. 2021;188(12):407. doi:10.1007/s00604-021-05054-y
- Zhou Y, Quan G, Wu Q, et al. Mesoporous silica nanoparticles for drug and gene delivery. *Acta Pharm Sin B*. 2018;8(2):165–177. doi:10.1016/j.apsb.2018.01.007
- Jafari S, Derakhshankhah H, Alaei L, Fattahi A, Varnamkhasti BS, Saboury AA. Mesoporous silica nanoparticles for therapeutic/diagnostic applications. *Biomed Pharma*. 2019;109:1100–1111. doi:10.1016/j.biopha.2018.10.167
- Sun X, Zhang J, Wang Z, Liu B, Zhu S, Zhu L. Licorice isoliquiritigenin-encapsulated mesoporous silica nanoparticles for osteoclast inhibition and bone loss prevention. *Theranostics*. 2019;9(18):5183–5199. doi:10.7150/thno.33376

27. Wang W, Meng Q, Li Q, et al. Chitosan derivatives and their application in biomedicine. *Int J Mol Sci.* 2020;21(2):487. doi:10.3390/ijms21020487
28. Lohiya G, Katti DS. Carboxylated chitosan-mediated improved efficacy of mesoporous silica nanoparticle-based targeted drug delivery system for breast cancer therapy. *Carbohydr Polym.* 2022;277:118822. doi:10.1016/j.carbpol.2021.118822
29. Tang F, Li L, Chen D. Mesoporous silica nanoparticles: synthesis, biocompatibility and drug delivery. *Adv Mater.* 2012;24(12):1504–1534. doi:10.1002/adma.201104763
30. Andreev D, Liu M, Weidner D, et al. Osteocyte necrosis triggers osteoclast-mediated bone loss through macrophage-inducible C-type lectin. *J Clin Invest.* 2020;130(9):4811–4830. doi:10.1172/JCI134214
31. Jiang G, Li S, Yu K, et al. A 3D-printed PRP-GelMA hydrogel promotes osteochondral regeneration through M2 macrophage polarization in a rabbit model. *Acta Biomater.* 2021;128:150–162. doi:10.1016/j.actbio.2021.04.010
32. Ono T, Nakashima T. Recent advances in osteoclast biology. *Histochem Cell Biol.* 2018;149(4):325–341. doi:10.1007/s00418-018-1636-2
33. Maaik B, Sebastian F, Nicholas A. Stimuli-responsive materials: a smart way to study dynamic cell responses. *Smart Mater Med.* 2022;12(3):257–273.
34. Marcoline FV, Ishida Y, Mindell JA, Nayak S, Grabe M. A mathematical model of osteoclast acidification during bone resorption. *Bone.* 2016;93:167–180. doi:10.1016/j.bone.2016.09.007
35. Huang DM, Hung Y, Ko BS, Hsu SC, Chen WH, Chien CL. Highly efficient cellular labeling of mesoporous nanoparticles in human mesenchymal stem cells: implication for stem cell tracking. *FASEB J.* 2005;19(14):2014–2016. doi:10.1096/fj.05-4288fje
36. Liu W, Dan X, Lu WW, et al. Spatial distribution of biomaterial microenvironment pH and its modulatory effect on osteoclasts at the early stage of bone defect regeneration. *ACS Appl Mater Interfac.* 2019;11(9):9557–9572. doi:10.1021/acsami.8b20580
37. Zhang S, Gao H, Bao G. Physical principles of nanoparticle cellular endocytosis. *ACS Nano.* 2015;9(9):8655–8671. doi:10.1021/acs.nano.5b03184
38. Kempen PJ, Greasley S, Parker KA, et al. Theranostic mesoporous silica nanoparticles biodegrade after pro-survival drug delivery and ultrasound/magnetic resonance imaging of stem cells. *Theranostics.* 2015;5(6):631–642. doi:10.7150/thno.11389
39. Mao S, Wang S, Niu Y, et al. Induction of cartilage regeneration by nanoparticles loaded with dentin matrix extracted proteins. *Tissue Eng Part A.* 2022;28(19–20):807–817. doi:10.1089/ten.TEA.2022.0049
40. Barati D, Gegg C, Yang F. Nanoparticle-Mediated TGF- β Release from Microribbon-Based Hydrogels Accelerates Stem Cell-Based Cartilage Formation In Vivo. *Ann Biomed Eng.* 2020;48(7):1971–1981. doi:10.1007/s10439-020-02522-z
41. Wei S, Wu H, Luo XJ. Biomimetic Precursor Carrier System Based on Carboxyl-Functionalized Large Pore Mesoporous Silica Nanoparticles. *Curr Med Sci.* 2020;40(1):155–167. doi:10.1007/s11596-020-2159-3
42. Tavares MT, Oliveira MB, Gaspar VM, Mano JF, Farinha JPS, Baleizão C. Efficient Single-Dose Induction of Osteogenic Differentiation of Stem Cells Using Multi-Bioactive Hybrid Nanocarriers. *Adv Biosyst.* 2020;4(11):2000123. doi:10.1002/adbi.202000123
43. Rizeq BR, Younes NN, Rasool K, Nasrallah GK. Synthesis, Bioapplications, and Toxicity Evaluation of Chitosan-Based Nanoparticles. *Int J Mol Sci.* 2019;20(22):5776. doi:10.3390/ijms20225776
44. Abou-Saleh H, Younes N, Rasool K, et al. Impaired Liver Size and Compromised Neurobehavioral Activity are Elicited by Chitosan Nanoparticles in the Zebrafish Embryo Model. *Nanomaterials.* 2019;9(1):122. doi:10.3390/nano9010122
45. Chen M, Hu Y, Hou Y, Li M, Chen M, Mu C. Differentiation regulation of mesenchymal stem cells via autophagy induced by structurally-different silica based nanobiomaterials. *J Mater Chem B.* 2019;7(16):2657. doi:10.1039/c9tb00040b
46. Shen Y, Shao Y, He H, Tan Y, Tian X, Xie F. Gadolinium(3+)-doped mesoporous silica nanoparticles as a potential magnetic resonance tracer for monitoring the migration of stem cells in vivo. *Int J Nanomed.* 2013;8:119–127. doi:10.2147/IJN.S38213
47. Aliprantis AO, Ueki Y, Sulyanto R, et al. NFATc1 in mice represses osteoprotegerin during osteoclastogenesis and dissociates systemic osteopenia from inflammation in cherubism. *J Clin Invest.* 2008;118(11):3775–3789. doi:10.1172/JCI35711
48. Tang Y, Luo K, Chen Y, et al. Phosphorylation inhibition of protein-tyrosine phosphatase 1B tyrosine-152 induces bone regeneration coupled with angiogenesis for bone tissue engineering. *Bioact Mater.* 2021;6(7):2039–2057. doi:10.1016/j.bioactmat.2020.12.025
49. Hu H, Dong L, Bu Z, et al. miR-23a-3p-abundant small extracellular vesicles released from Gelma/nanoclay hydrogel for cartilage regeneration. *J Extracell Vesicles.* 2020;9(1):1778883. doi:10.1080/20013078.2020.1778883

International Journal of Nanomedicine

Dovepress

Publish your work in this journal

The International Journal of Nanomedicine is an international, peer-reviewed journal focusing on the application of nanotechnology in diagnostics, therapeutics, and drug delivery systems throughout the biomedical field. This journal is indexed on PubMed Central, MedLine, CAS, SciSearch®, Current Contents®/Clinical Medicine, Journal Citation Reports/Science Edition, EMBASE, Scopus and the Elsevier Bibliographic databases. The manuscript management system is completely online and includes a very quick and fair peer-review system, which is all easy to use. Visit <http://www.dovepress.com/testimonials.php> to read real quotes from published authors.

Submit your manuscript here: <https://www.dovepress.com/international-journal-of-nanomedicine-journal>